The Astrophysical Journal, 762:46 (24pp), 2013 January 1 doi:10.1088/0004-637X/762/1/46

SHARDS: AN OPTICAL SPECTRO-PHOTOMETRIC SURVEY OF DISTANT GALAXIES

Pablo G. Pérez-González[1,18], Antonio Cava[1], Guillermo Barro[1,2], Víctor Villar[1], Nicolás Cardiel[1], Ignacio Ferreras[3], José Miguel Rodríguez-Espinosa[4,5], Almudena Alonso-Herrero[6,19], Marc Balcells[4,5,7], Javier Cenarro[8], Jordi Cepa[4,5], Stéphane Charlot[9], Andrea Cimatti[10], Christopher J. Conselice[11], Emmanuele Daddi[12], Jennifer Donley[13], David Elbaz[12], Néstor Espino[1], Jesús Gallego[1], R. Gobat[14], Omaira González-Martín[4,5], Rafael Guzmán[15], Antonio Hernán-Caballero[6], Casiana Muñoz-Tuñón[4,5], Alvio Renzini[16], Javier Rodríguez-Zaurín[4,5], Laurence Tresse[17], Ignacio Trujillo[4,5], and Jaime Zamorano[1]
[1] Departamento de Astrofísica, Facultad de CC. Físicas, Universidad Complutense de Madrid, E-28040 Madrid, Spain
[2] UCO/Lick Observatory, Department of Astronomy and Astrophysics, University of California, Santa Cruz, CA 95064, USA
[3] Mullard Space Science Laboratory, University College London, Holmbury St Mary, Dorking, Surrey RH5 6NT, UK
[4] Instituto de Astrofísica de Canarias, E-38200 La Laguna, Tenerife, Spain
[5] Departamento de Astrofísica, Universidad de La Laguna, E-38205 La Laguna, Tenerife, Spain
[6] Instituto de Física de Cantabria, CSIC-Universidad de Cantabria, E-39005 Santander, Spain
[7] Isaac Newton Group of Telescopes, Apdo. 321, E-38700 Santa Cruz de La Palma, Spain
[8] Centro de Estudios de Física del Cosmos de Aragón, Plaza San Juan 1, Planta 2, E-44001 Teruel, Spain
[9] Institut d'Astrophysique de Paris, CNRS, Université Pierre & Marie Curie, UMR 7095, 98bis bd Arago, F-75014 Paris, France
[10] Dipartimento di Astronomia, Universitá degli Studi di Bologna, I-40127 Bologna, Italy
[11] School of Physics & Astronomy, University of Nottingham, Nottingham NG7 2RD, UK
[12] CEA, Laboratoire AIM, Irfu/SAp, F-91191 Gif-sur-Yvette, France
[13] Los Alamos National Laboratory, Los Alamos, NM, USA
[14] Laboratoire AIM-Paris-Saclay, CEA/DSM-CNRS-Université Paris Diderot, Irfu/Service d'Astrophysique, CEA Saclay, Orme des Merisiers, F-91191 Gif-sur-Yvette, France
[15] Department of Astronomy, University of Florida, 211 Bryant Space Science Center, Gainesville, FL 32611, USA
[16] INAF-Osservatorio Astronomico di Padova, Vicolo dell'Osservatorio 5, I-35122 Padova, Italy
[17] Aix Marseille Université, CNRS, LAM (Laboratoire d'Astrophysique de Marseille), UMR 7326, F-13388 Marseille, France
Received 2012 July 26; accepted 2012 October 23; published 2012 December 14

ABSTRACT

We present the Survey for High-z Absorption Red and Dead Sources (SHARDS), an ESO/GTC Large Program carried out using the OSIRIS instrument on the 10.4 m Gran Telescopio Canarias (GTC). SHARDS is an ultra-deep optical spectro-photometric survey of the GOODS-N field covering 130 arcmin^2 at wavelengths between 500 and 950 nm with 24 contiguous medium-band filters (providing a spectral resolution $R \sim 50$). The data reach an AB magnitude of 26.5 (at least at a 3σ level) with sub-arcsec seeing in all bands. SHARDS' main goal is to obtain accurate physical properties of intermediate- and high-z galaxies using well-sampled optical spectral energy distributions (SEDs) with sufficient spectral resolution to measure absorption and emission features, whose analysis will provide reliable stellar population and active galactic nucleus (AGN) parameters. Among the different populations of high-z galaxies, SHARDS' principal targets are massive quiescent galaxies at $z > 1$, whose existence is one of the major challenges facing current hierarchical models of galaxy formation. In this paper, we outline the observational strategy and include a detailed discussion of the special reduction and calibration procedures which should be applied to the GTC/OSIRIS data. An assessment of the SHARDS data quality is also performed. We present science demonstration results on the detection and study of emission-line galaxies (star-forming objects and AGNs) at $z = 0$–5. We also analyze the SEDs for a sample of 27 quiescent massive galaxies with spectroscopic redshifts in the range $1.0 < z \lesssim 1.4$. We discuss the improvements introduced by the SHARDS data set in the analysis of their star formation history and stellar properties. We discuss the systematics arising from the use of different stellar population libraries, typical in this kind of study. Averaging the results from the different libraries, we find that the UV-to-MIR SEDs of the massive quiescent galaxies at $z = 1.0$–1.4 are well described by an exponentially decaying star formation history with scale $\tau = 100$–200 Myr, age around 1.5–2.0 Gyr, solar or slightly sub-solar metallicity, and moderate extinction, $A(V) \sim 0.5$ mag. We also find that galaxies with masses above M^* are typically older than lighter galaxies, as expected in a downsizing scenario of galaxy formation. This trend is, however, model dependent, i.e., it is significantly more evident in the results obtained with some stellar population synthesis libraries, and almost absent in others.

Key words: galaxies: high-redshift – galaxies: photometry – galaxies: starburst – infrared: galaxies

Online-only material: color figures, machine-readable table

1. INTRODUCTION

The current paradigm of galaxy formation establishes that baryons closely follow the evolution of the cold dark matter (CDM) halos, which cluster and grow hierarchically as shown in cosmological simulations and semi-analytical models (such as those in Springel et al. 2005; see also Baugh et al. 1998; Somerville & Primack 1999; Cole et al. 2000; Somerville et al. 2008; Ricciardelli & Franceschini 2010). In this scenario, star formation started within the cooling gas clouds in merging dark matter halos after a relatively slow early collapse regulated by feedback processes. This early star

[18] Associate Astronomer at Steward Observatory, The University of Arizona.
[19] Augusto González Linares Senior Research Fellow.

formation produced relatively small disk systems that later merged and generated larger (i.e., more massive) spheroidal systems (see, e.g., Kauffmann et al. 1993; Ellis et al. 2000, 2001).

The global picture of the co-evolution of matter in the universe (including all gravity components: CDM and baryons) is self-consistent and has been successful in reproducing and even predicting many observables about galaxy evolution, especially at low redshift. Among the most relevant successes, we find the good comparison of models with the observed power spectrum of the cosmic microwave background (Spergel et al. 2007; Komatsu et al. 2011) or the large-scale structure of the universe (Percival et al. 2001; Colless et al. 2001). Also very convincing is the link between observations and theoretical expectations such as the existence and properties of acoustic baryonic oscillations (Eisenstein et al. 2005; Gaztañaga et al. 2009; Percival et al. 2010). In addition, the hierarchical scenario for galaxy formation is supported by the observations of galaxy mergers at different cosmological distances (e.g., van Dokkum et al. 1999; van Dokkum 2005; Miley et al. 2006), and the increase of the fraction of galaxies undergoing mergers as we move to higher redshifts (see, for example, Lacey & Cole 1993; Le Fèvre et al. 2000; Conselice et al. 2003; Bell et al. 2006; Lotz et al. 2008; López-Sanjuan et al. 2009).

However, the hierarchical picture contrasts with several pieces of observational evidence, especially at high redshift ($z >$ 1–2), where a more classical monolithic collapse is favored. This formation path was proposed 50 years ago to explain the origin of bulges such as the Milky Way's and spheroidal galaxies. This would occur through a free-fall rapid collapse causing the formation of the bulk of the stars in these systems in a short period of time. Later, the star formation is shut off by some *quenching* phenomena, and the galaxy henceforth evolves passively (Eggen et al. 1962; Larson 1974). This theory was largely abandoned due to the compilation of evidence supporting that spheroidal galaxies suffer merging episodes (Toomre & Toomre 1972). Furthermore, globular clusters and the general stellar population in the Milky Way present a relatively wide range of ages (e.g., Searle & Zinn 1978), directly pointing to the hierarchical scenario. Eventually, the hierarchical picture was adopted instead of monolithic collapse due to the high degree of success of the ΛCDM and semi-analytic models mentioned above.

Nevertheless, rapid early episodes of intense star formation are indeed consistent (although not uniquely) with observational facts in nearby galaxies, such as the dominant old stellar populations in bulges and ellipticals, their metallicity and α-element enhancement, and the dynamics and shape of these systems (e.g., Vazdekis et al. 1997; Faber et al. 1997; Trager et al. 2000a, 2000b). In addition, hierarchical models still present severe drawbacks in several aspects. The most challenging observational facts for hierarchical models refer to the lightest and heaviest galaxies. Indeed, hierarchical models typically present a "missing satellite problem," i.e., they predict many more low-mass galaxies than are actually observed (see Kauffmann et al. 1993, 1999; Klypin et al. 1999; Kravtsov et al. 2004; Li & White 2009; Quilis & Trujillo 2012). At the bright end, models tend also to overpredict the number of massive galaxies observed in the local universe, although they are getting closer to the observations after taking into account quenching mechanisms (Croton et al. 2006; De Lucia & Blaizot 2007; Somerville et al. 2008; Ricciardelli & Franceschini 2010; Guo et al. 2010).

The discrepancies between the predictions of current galaxy formation models based on the ΛCDM paradigm and the data are more obvious as we move to higher redshifts. Over the last 15 years, a wide variety of papers using very heterogeneous data and methods have presented compelling evidence that the formation of galaxies follows a so-called *downsizing* scenario (Cowie et al. 1996; Heavens et al. 2004; Glazebrook et al. 2004; Bauer et al. 2005; Pérez-González et al. 2005, 2008; Arnouts et al. 2007). In this theory, the most massive galaxies formed first in the history of the universe, and thus have the oldest stellar populations seen today. The formation of less massive systems continued at lower redshifts. Downsizing implies that the bulk of the star formation in the most massive galaxies happened rapidly and stopped for some reason at early times. This also means that there should be massive passively evolving galaxies at high redshift. These kinds of objects have indeed been detected at redshifts around $z \sim$ 1–3 using a variety of techniques (Yan et al. 2000; Franx et al. 2003; Daddi et al. 2004; Papovich et al. 2006; Cimatti et al. 2008).

The discovery of massive galaxies at $z =$ 1–3, some of them already evolving passively, is indeed extremely challenging for current models of galaxy formation based on the ΛCDM paradigm. Indeed, models predict a smaller number density of massive systems at high-z than observed (see, e.g., Conselice et al. 2007; Marchesini et al. 2009; Henriques et al. 2012; Leauthaud et al. 2012). In contrast, the downsizing scenario contradicts, at least at first sight, the predictions of a hierarchical assembly of the stellar mass in galaxies, i.e., the most massive galaxies do not seem to be the result of multiple mergers occurring in an extended period along the Hubble time (Baugh et al. 1998; Cole et al. 2000; Faber et al. 2007). Still, a hierarchical assembly with (maybe multiple) mergers occurring at high redshift between gas-rich systems (a process close in nature to a monolithic collapse) would be consistent with both the evidence for downsizing and the properties of the dominant stellar populations seen in nearby spheroidal systems (e.g. Dekel et al. 2009).

From the observational point of view, our understanding of the processes involved in the early ($z > 1$) assembly of galaxies (and also the evolution from the early universe to the present) is still hampered by significant (often systematic) uncertainties in our estimations of their physical properties. Our global picture of galaxy formation will only improve if we are able to obtain more robust estimations of some key properties of galaxies, such as the stellar masses, star formation rates (SFRs), and extinctions. Jointly with those, we of course need better estimations of the distances to galaxies based on spectroscopic or photometric redshifts, which can then be used to relate the aforementioned galaxy properties to other relevant parameters such as the environment. Improvements in the determination of stellar masses and SFRs/extinctions will also lead to a better estimation of the age of the stellar population and the star formation history, SFH (see, e.g., Papovich et al. 2001; Fontana et al. 2006; Kriek et al. 2008; Elsner et al. 2008; Pforr et al. 2012; Pacifici et al. 2012). Along with this observational effort, models should also be improved to include better physics. For example, models need to provide more certain emissivities of the stellar populations in the rest-frame NIR, currently affected by strong uncertainties due to limitations of knowledge of the properties and importance of stellar evolutionary phases such as the thermally pulsating asymptotic giant branch (TP-AGB) phase (see Maraston 2005; Kriek et al. 2010). The task of obtaining more robust physical parameters of galaxies at cosmological

distances is even more interesting for those massive galaxies which have already reached a quiescent state and are evolving passively at high-z, and whose number densities and properties are the most demanding challenges for current galaxy evolution models. The cosmological importance of these systems is very high, since they most probably represent the early formation phases of present-day early-type galaxies.

In this paper, we present the basics of the Survey for High-z Absorption Red and Dead Sources (SHARDS), an ESO/GTC Large Program awarded 180 hr of GTC/OSIRIS time during 2010–2013. This project consists of an ultra-deep ($m < 26.5$ AB mag) imaging survey in 24 medium-band filters, covering the wavelength range between 500 and 950 nm and targeting the GOODS-N field. The observations carried out by SHARDS allow us to accurately determine the main properties of the stellar populations present in these galaxies through spectro-photometric data with a resolution $R \sim 50$, sufficient to measure absorption indices such as the $D(4000)$ (e.g., Bruzual 1983; Balogh et al. 1999; Kauffmann et al. 2003a; Kriek et al. 2011) or Mg_{UV} index (Spinrad et al. 1997; McCarthy et al. 2004; Saracco et al. 2005; Daddi et al. 2005b; Cimatti et al. 2008). Analysis of these spectral features is a powerful method for constraining the solutions of stellar population synthesis (SPS) models and improving our estimations of parameters such as the age, SFH, mass, and extinction of galaxies at cosmological distances.

SHARDS inherits the observational strategy of past and ongoing optical surveys such as COMBO17 (Wolf et al. 2001, 2003), the COSMOS medium-band survey (Ilbert et al. 2009), ALHAMBRA (Moles et al. 2008), and PAU/J-PAS (Benítez et al. 2009a; Abramo et al. 2011). These projects have demonstrated the impact of large photometric data sets on our understanding of the formation of galaxies (see, among many papers, Bell et al. 2004; Faber et al. 2007; Wolf et al. 2004; Rix et al. 2004; Borch et al. 2006; Caputi et al. 2006; Scoville et al. 2007; Benítez et al. 2009b; Cardamone et al. 2010; Whitaker et al. 2011). SHARDS intends to be a step forward from these surveys in terms of depth, spectral resolution, and data quality. Our survey prioritizes the detailed study of the faintest galaxies at the highest redshifts over the analysis of closer galaxy populations and the large-scale structure at intermediate redshift, and thus focuses on a smaller area than the surveys mentioned above. Indeed, SHARDS was planned to reach up to 3 mag fainter than those surveys, uses typically twice the number of filters in the same wavelength range (i.e., our spectral resolution is better), and the observations were made in excellent (sub-arcsec) seeing conditions with a 10 m class telescope. In contrast, it covers a fraction of the area surveyed by other projects.

In this paper, we present the main technical characteristics of the survey in Section 2, and a thorough discussion of the reduction and calibration procedures in Section 3. Next, we present our science verification results on emission-line and absorption systems. In Sections 4.1 and 4.2, we discuss the ability of the SHARDS data to select and study emission-line sources (star-forming galaxies and AGNs) at intermediate ($z < 1$) and high redshifts (up to $z \sim 5$ and beyond). In Section 5, we present detailed spectral energy distributions (SEDs) of massive quiescent galaxies at $z > 1$, and demonstrate the power of our spectro-photometric data to analyze the stellar populations in this kind of object through a detailed comparison with SPS models.

Throughout this paper we use AB magnitudes. We adopt the cosmology $H_0 = 70$ km s^{-1} Mpc^{-1}, $\Omega_m = 0.3$, and $\Omega_\lambda = 0.7$.

2. SURVEY DESCRIPTION

SHARDS is a medium-band optical survey currently being carried out with the Spanish 10.4 m telescope, Gran Telescopio Canarias (GTC), and its OSIRIS instrument. SHARDS was approved in 2010 as an ESO/GTC Large Program and awarded 180 hr of observing time to obtain data through 24 contiguous medium-band filters covering the wavelength range between 500 and 950 nm. The survey targets the GOODS-N field, covering most of the area observed with the *Hubble Space Telescope* (*HST*)/ACS instrument. SHARDS was conceived to study in detail the properties of the stellar populations in $0 < z < 4$ galaxies (and beyond), focusing on the major goal of analyzing quiescent massive galaxies at $z = 1.0$–2.5. To achieve this goal, the survey was planned to obtain photometric data in as many filters as necessary to cover the entire optical window with enough spectral resolution to be able to reliably measure absorption indices which could be used to perform a detailed and robust SPS. Indices such as $D(4000)$ or Mg_{UV} use spectral windows 10–20 nm wide. To obtain this spectral resolution (or better) at $z > 1$, we imposed filter widths of approximately 15–20 nm. A compromise between spectral resolution, depth, and manufacturing limitations was adopted and the survey was designed to use 17 nm wide filters. The bright night sky at wavelengths beyond ~800 nm imposes that filters as narrow as 17 nm would not reach the required magnitude limit to study high-z sources, so our two reddest filters are twice as wide. SHARDS was conceived to reach typical magnitudes of sub-L^* galaxies at $z > 1$ for every single filter, so the goal was to obtain a depth of 26.5–27.0 mag at the 3σ level with sub-arcsec seeing. The final manufacturing process resulted in an average width for our filter set of around 15–16 nm, except for the two reddest filters, which had a width of 33–35 nm. Figure 1 shows the layout of the filter set and the observational strategy of SHARDS. The characteristics of the filters (for the ones with available data in 2012A) are given in Table 1, along with other details of the SHARDS data.

SHARDS is carried out in the GOODS-N field, one of the most targeted areas of the sky at all wavelengths. Virtually all the deep region covered by the ACS is surveyed by SHARDS using two OSIRIS pointings, summing up a total surveyed area of ~130 arcmin^2 (see Figure 2). The central J2000 coordinates of the two pointings are $\alpha = 12{:}37{:}18.9$, $\delta = +62{:}17{:}03$ and $\alpha = 12{:}36{:}33.3$, $\delta = +62{:}11{:}39$. A position angle of 45° was used for our imaging data in order to cover the GOODS-N region more efficiently.

The multi-wavelength data set available in GOODS-N is extensive, ranging from an ultra-deep X-ray exposure to the deepest data in the MIR/FIR with surveys such as FIDEL (Frayer et al. 2006), PEP (Lutz et al. 2011), HerMES (Oliver et al. 2010), or *Herschel*-GOODS (Elbaz et al. 2011), as well as multiple spectroscopic redshifts (Wirth et al. 2004; Cowie et al. 2004; Reddy et al. 2006), a few of them at $z > 1.5$ (Reddy et al. 2005; Barger et al. 2008). Closely complementary to the SHARDS data, GOODS-N has been observed by *HST* with the ACS and WFC3 (see Figure 2) providing slitless, intermediate-resolution spectroscopy in the optical (through the G800L grism; PEARS, Kümmel et al. 2009; see also Pirzkal et al. 2004, 2009) and NIR (G141; PI: B. Weiner). GOODS-N is also one of the two fields counting with the deepest exposures taken by the GOODS (Giavalisco et al. 2004) and CANDELS (Grogin et al. 2011; Koekemoer et al. 2011) projects. In addition, the availability of the sky deepest IRAC ([3.6] < 26.0 mag) and MIPS [$F_{5\sigma}(24) > 30\,\mu$Jy] observations ensures the detection of

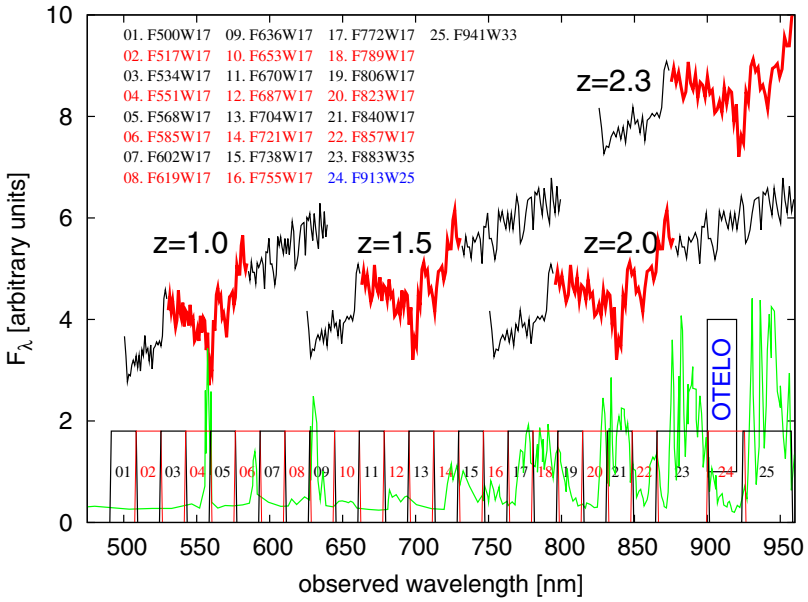

Figure 1. Observing strategy of SHARDS. The figure shows a scheme of the transmission curves for the 24 SHARDS medium-band filters (black and red lines at the bottom, with names giving nominal central wavelengths and widths, as written in the legend). This filter set was designed to probe the optical wavelength range contiguously between 500 and 950 nm with filters of width FWHM $\sim$ 17 nm (spectral resolution $R \sim 50$). The observing strategy of SHARDS was devised to identify quiescent galaxies at $z > 1$. We show how the stacked spectrum of the 13 spectroscopically confirmed quiescent massive galaxies at $1.4 < z < 2.0$ in GOODS-S (Cimatti et al. 2008; the stack takes up 480 hr of Very Large Telescope time) would look at four different redshifts. The sky spectrum is also depicted in green. Using 24 filters, SHARDS probes the prominent absorption feature located at $\lambda = 265$–295 nm, distinctive of passively evolving galaxies (marked in red) with a resolution $R \sim 50$, and is able to measure its strength using a spectro-photometric technique to accurately determine stellar age and distance for individual high-z galaxies. The 900 nm atmospheric window is not covered by our survey, since it will be studied by another approved GTC Guaranteed Time project (OTELO; Cepa et al. 2011; Lara-López et al. 2011).

(A color version of this figure is available in the online journal.)

Table 1
Characteristics of the SHARDS Filter Set and Observations (Before 2012A)

Filter	CWL	Width	A	B	X_0	Y_0	rms	ΔZP		$m_{3\sigma}$		$m_{75\%}$		Seeing	
								P1	P2	P1	P2	P1	P2	P1	P2
(1)	(2)	(3)	(4)	(5)	(6)	(7)	(8)	(9)	(9)	(10)	(10)	(11)	(11)	(12)	(12)
F619W17	618.9	15.1	623.14	−2.402e-6	−202	985	0.10	0.077	...	26.89	...	27.22	...	0.85	...
F636W17	638.4	15.4	641.37	−2.587e-6	−116	986	0.10	0.066	0.072	26.78	26.70	27.15	27.17	0.79	0.92
F653W17	653.1	14.8	656.01	−2.634e-6	−151	999	0.10	0.063	0.065	26.91	27.07	27.17	27.15	0.98	1.00
F670W17	668.4	15.3	671.86	−2.600e-6	−183	1037	0.10	0.062	0.064	26.64	26.76	27.12	27.18	0.79	1.07
F687W17	688.2	15.3	690.50	−2.674e-6	−186	983	0.10	0.050	0.055	27.04	26.85	27.10	27.09	0.84	0.93
F704W17	704.5	17.1	707.78	−2.723e-6	−209	1028	0.10	0.055	0.063	26.71	26.63	27.01	26.95	0.89	0.92
F721W17	720.2	18.2	723.12	−2.969e-6	−94	960	0.10	0.056	0.060	26.60	26.51	26.97	26.96	0.93	1.02
F738W17	737.8	15.0	741.80	−2.411e-6	−328	1050	0.10	0.050	0.061	26.45	26.25	26.95	26.87	0.86	0.90
F755W17	754.5	14.8	758.12	−2.660e-6	−228	1034	0.10	0.050	0.055	26.69	26.37	26.93	26.91	0.92	0.93
F772W17	770.9	15.4	774.62	−2.929e-6	−122	1026	0.10	0.054	0.053	26.54	26.34	26.90	26.83	0.94	1.04
F789W17	789.0	15.5	791.22	−3.087e-6	−123	994	0.10	0.054	0.056	26.22	26.02	26.84	26.63	0.97	0.92
F806W17	805.6	15.6	809.42	−2.939e-6	−200	933	0.10	0.051	0.050	26.39	26.38	26.82	26.77	0.96	0.99
F823W17	825.4	14.7	829.15	−3.055e-6	−153	888	0.10	0.049	0.049	26.59	26.65	26.91	26.89	0.82	0.91
F840W17	840.0	15.4	843.51	−3.103e-6	−237	992	0.10	0.057	0.056	26.13	26.19	26.79	26.74	0.88	0.91
F857W17	856.4	15.8	859.97	−2.892e-6	−249	1002	0.10	0.050	0.051	26.84	26.23	26.88	26.63	0.73	0.95
F883W35	880.3	31.7	885.33	−2.889e-6	−285	978	0.10	0.065	0.057	26.06	26.06	26.64	26.58	0.93	1.02

Notes. (1) Filter name. (2) Central wavelength (in nm) of the filter for angle of incidence AOI = 10.°5 (approximately that for the center of the FOV). (3) Filter width (in nm). (4) Coefficient A (in nm) for CWL calibration (from Equation (1)). (5) Coefficient B (in pixel^{-2}) for CWL calibration (from Equation (1)). (6) X coordinate for the OSIRIS optical center (in pixels). (7) Y coordinate for the OSIRIS optical center (in pixels). (8) rms of the CWL calibration (in nm). (9) Zero-point uncertainty for pointings 1 and 2. (10) Sensitivity limit at 3σ level (AB mag) for pointings 1 and 2. (11) Third quartile of the magnitude distribution (AB mag) for pointings 1 and 2. (12) Average seeing (in arcsec) for pointings 1 and 2.

the rest-frame NIR/MIR emission of the galaxies and allows us to robustly estimate stellar masses and SFRs (Pérez-González et al. 2005, 2008; Cimatti et al. 2008). This wealth of data converts GOODS-N in one of the two best fields (the other being GOODS-S) for the study of the first galaxies and their evolution, and the best in the northern sky hemisphere.

At the time of publication of this paper, 75% of the SHARDS data have already been collected. Table 1 presents the data

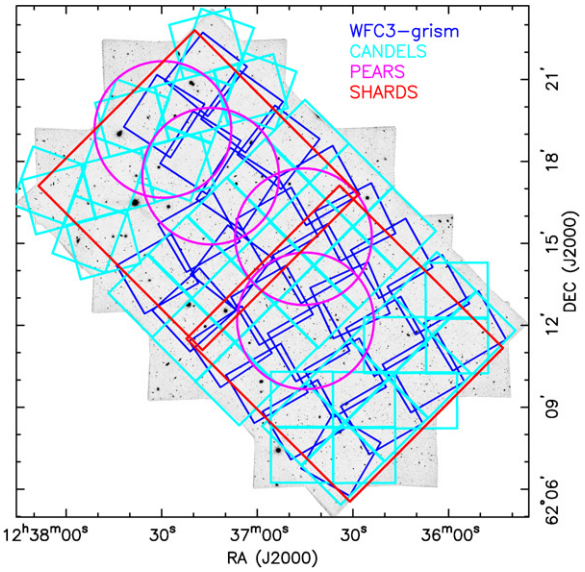

Figure 2. Footprint of the SHARDS data superimposed on the ACS images for the GOODS-N field. The footprints of the *HST* grism surveys carried out with ACS (PEARS) and WFC3 (PI: Weiner) and the CANDELS coverage of GOODS-N are also shown. SHARDS covers a total surveyed area of $\sim$130 arcmin^2 divided into two pointings.

(A color version of this figure is available in the online journal.)

characteristics for the observed filters in the two SHARDS pointings.

3. DATA REDUCTION AND CALIBRATION

3.1. Reduction Pipeline

The GTC/OSIRIS instrument (Cepa 2010) is an optical imager equipped with two CCDs, which cover a total (usable) field of view (FOV) of $7\farcm4 \times 8\farcm4$. There is a gap between the two detectors, of size $10''$–$12''$ as measured directly in our images in different locations along the gap and after masking non-useful pixels and correcting for distortions. OSIRIS presents special characteristics which should be taken into account in the data reduction procedure. Consequently, apart from the standard reduction steps (bias subtraction and flat fielding), our custom OSIRIS pipeline includes the following additional steps: illumination correction, background gradient subtraction, fringing removal, World Coordinate System (WCS) alignment taking into account field distortions, and two-dimensional calibration of the photometric passband and zero point. In what follows, we elaborate on these steps and describe in detail the non-standard parts of the reduction.

Bias frames were taken each night. These calibration data were found to be very stable and uniform, with typical variations of less than 3% from pixel to pixel and from night to night. Dark current was found to be negligible in all our data.

Sky flats for each filter in the SHARDS data set were taken at sunset and dawn every night. These flats presented strong gradients across the field (typically, 10%–50% differences in brightness from one edge of the FOV to another), with significant spatial and temporal brightness variations. These gradients were also seen in science data during both dark and (especially) gray night-time. A systematic 3% offset between the sensitivity of the two CCDs in OSIRIS was also detected (and corrected by our pipeline).

After analyzing night- and day-time data, we concluded that these spatial variations were mainly due to the special characteristics of the OSIRIS instrument, which operates off-axis for our observational setup (medium- and broad-band imaging). Indeed, light rays reach the OSIRIS detector (when not using the tunable filters) in a wide range of angles of incidence (AOI): $-2^\circ \lesssim \mathrm{AOI} \lesssim 22^\circ$. Given the typical dependence on the light ray's AOI of the central wavelength (CWL) of the passband for interference filters, and the medium width of our filter set, our flat-field frames were subject to the spectral features of the sky spectrum, and their temporal variations.

The optical axis is outside the OSIRIS FOV when using a single broad- or medium-band filter (cf. columns 6 and 7 in Table 1). For this reason, a gradient is observed in our data (flat-field and science images) with a symmetry around a horizontal line approximately dissecting into equal parts the FOV in the vertical direction. The gradient follows a radial profile centered in the optical axis. It presents varying structures of different brightnesses whose position and strength depend on time and on the filter. The brightest structures are located where strong sky emission lines (or bands) go through the passband for each physical filter as its CWL is changing along the FOV.

This effect directly related to the special characteristics of OSIRIS and our instrumental setup means that it is very difficult to find a spatially constant light source to take flat fields, i.e., a significant part of the structure of the flat-field frames is linked to the sky spectrum. Thus, our pipeline included an illumination correction to get rid of this effect as much as possible. This illumination correction was carried out by comparing the flat-field images taken for our medium-band filters with those acquired through broad band passbands (typically, *r*- and *i*-band filters). For these broad band filters, the sky spectrum is averaged in a spectral range which is wide enough to prevent strong spatial variations, and is also very constant in time. Indeed, the super-skyflat provided by the observatory, and built with thousands of frames, shows variations of less than 5% along the FOV and from night to night.

We used the ratio of our medium-band flat fields to the broadband flat fields to correct the SHARDS data for the illumination effect. These ratios were smoothed using a third-order spline.

After applying the flat-field and illumination corrections to the science data, these images presented a highly symmetric sky gradient, which was subtracted with a median filtering and spline interpolation, after masking objects. In order to avoid the effect of the wings of the objects in this sky determination, we increased the extension of the sources (typically by a factor of two in Kron radius; Kron 1980) taking into account their brightnesses, and we also masked out faint objects detected in a preliminary mosaic constructed for each filter by adding all the available observations.

The data for the filters whose CWLs are redder than $\sim$700 nm presented some fringing (typically with an intensity below 1% of the background). We removed this additive effect using the RMFRINGE task in IRAF.[20]

Before stacking all the data together, we calibrated the WCS for each image using the positions of several hundred objects for each CCD, which were cross-correlated with a sample of galaxies detected in the Subaru *R*-band image of GOODS-N. For this task, we used the SCamp program (Bertin 2006), and the WCS utilities in IRAF, obtaining for each frame an undistorted

[20] IRAF is distributed by the National Optical Astronomy Observatory, which is operated by the Association of Universities for Research in Astronomy (AURA) under cooperative agreement with the National Science Foundation.

image remapped to a TAN-SIP coordinate system. The distortion in individual frames reached several arcseconds in the edges, and the final WCS calibrated images presented a typical position uncertainty around 0.″1 throughout the FOV.

Finally, the SHARDS pipeline stacks together all the data for a given filter with a sigma-clipping algorithm to get rid of cosmic rays and artifacts, producing final mosaics and exposure maps with the same WCS for all SHARDS filters and for each of our two pointings covering the GOODS-N field.

3.2. Calibration Procedures

Given the special characteristics of the OSIRIS instrument at GTC, within each single frame taken with a given physical filter, each pixel sees a different passband. This has a strong effect on the images taken with medium-band filters, where the shift of the CWL of the actual passband seen by different parts of the detector produces sky gradients and significant difficulties in obtaining flat-field calibration images, as explained in the previous section. To overcome this issue, we performed a detailed calibration of the effective passband and photometric zero point as a function of the position in the FOV. Although part of the spatial variation of the photometric zero point can be removed by applying an illumination correction built with broad-band flat-field images, a small effect can remain in the images. To account for this, during our calibration procedure we considered that the zero point could vary along the image. The calibration method was devised, consequently, to determine the spatial variation of the zero point. Note that after the calibration routine, we can construct a photometric catalog for each physical filter, but within this catalog, the flux measurements for each detected source refer to a different passband. This is quite different from a standard photometric catalog for a given physical filter, where all sources share the same passband.

We describe the procedures to carry out the calibration of the SHARDS data in the following subsections, starting from the CWL calibration and following with the absolute flux calibration.

3.3. Passband Central Wavelength (CWL) Calibration

The CWL of the passband seen by different parts of the OSIRIS detector for a given physical filter varies along the FOV. This dependence was calibrated with day-time imaging and spectroscopic data taken in the laboratory and at the GTC. In the lab, we calibrated the transmission curve for each filter as a function of the AOI of the incoming beam. At the telescope, once the given filter was mounted in OSIRIS, we took spectroscopic data through a special mask with 105 pinholes homogeneously covering the entire FOV. The positions of those pinholes were determined with images taken through the mask and using one of our filters. Then, we also took spectra of these pinholes with the R1000B and R1000R grisms (which cover the entire wavelength range probed by SHARDS) through our filters, calibrating them with Ne, HgAr, Xe, and Kr arcs. Typical uncertainties in the wavelength solution were smaller than 0.01 nm. These data were used to measure the transmission curve at each pinhole position. We characterized each curve using two parameters: the CWL and the width of the passband. The shape and width of the passbands are relatively independent of the position in the FOV (i.e., all pinholes show similar values within 0.2 nm). However, the CWL shows a significant symmetric variation around the optical axis, located to the left of the FOV. The CWLs for all the pinholes were fitted with a function depending

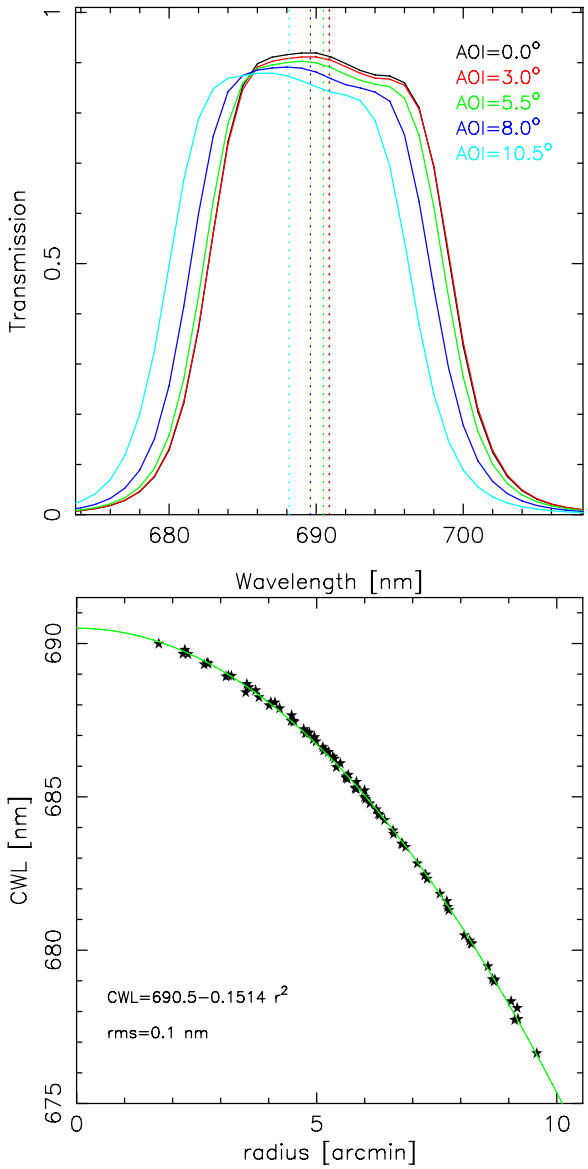

Figure 3. Top: calibration of the transmission curve of the F687W17 filter as a function of angle of incidence, obtained with laboratory data. The central wavelengths of each passband are marked with vertical lines. Bottom: calibration of the spatial variation of the CWL of the F687W17 filter along the OSIRIS FOV. This variation is symmetric and only depends on the distance to the optical axis. The data are fitted with the function in Equation (1) (green line), leaving the position of the optical axis as a fitting parameter. The best fit between CWL and distance to the optical axis in arcmin is given in the plot, along with its rms. The width of the passbands is relatively independent (differences within 0.2 nm) of the position in the FOV.

(A color version of this figure is available in the online journal.)

on the square of the distance to the optical axis (r^2), leaving also the position of the optical axis as a parameter to fit (see Méndez-Abreu et al. 2011 and Mayya et al. 2012 for a similar calibration procedure, but for the OSIRIS red tunable filter). An example of the calibration for one of the SHARDS filters is shown in Figure 3. The data were fitted with the following function:

$$\mathrm{CWL}(X, Y) = A + B \times [(X - X_0)^2 + (Y - Y_0)^2], \quad (1)$$

where X and Y are the positions (in pixels) in the OSIRIS FOV, and X_0 and Y_0 are the position of the optical axis, all of them combined to give the distance to the optical axis in pixels. X_0,

Y_0, A, and B were measured for each of the SHARDS filters by fitting the data described above and shown in Figure 3 for filter F687W17. When applied to the actual science data, the optical axis position was converted to R.A. and decl., and the distances were measured in arcmin using the nominal pixel size of our data, 0.251 arcsec pixel^{-1}.

The fitting coefficients in Equation (1) for each of the SHARDS filters (with available data so far) are given in Table 1. We remark that the four parameters in Equation (1) are highly correlated. Consequently, the differences seen from filter to filter may not be closely related to real differences in the position of the optical axis or CWL variation coefficients. In any case, we are only interested in recovering CWL values for any position within the FOV, and even assuming large (correlated) uncertainties for the four parameters, the results given in Table 1 do provide very accurate CWLs. In addition, we tested the repeatability of these measurements and no significant changes in this calibration were detected for observations taken in different nights.

3.4. Photometric Calibration

The significant variation of the passband seen by each point of the detector as a function of the position in the FOV implies a complex behavior of the absolute photometric calibration of the SHARDS images. Moreover, the effects of this CWL variation on the construction of the flat field (explained in Section 3.1) may also affect the flux calibration of the final mosaics (see Mayya et al. 2012 for a description of the same problem, but for the OSIRIS tunable filters). To cope with these issues, we developed a special flux calibration procedure, aimed at determining the zero point of the SHARDS mosaics in each filter as a function of position in the image. Note that the behavior of the passband is symmetric around the optical axis and each position in the FOV is characterized by a CWL (as explained in Section 3.3 and defined by Equation (1)). Keeping this in mind, we work with zero point variations as a function of CWL, instead of directly relating the calibration to a position in the images.

The flux calibration of the SHARDS mosaics was performed by comparing the measured photometry in our images with spectroscopic data for several sources in the field (most of them being galaxies). Given the need for spectroscopic calibration data for sources covering the whole FOV, direct observations taken with GTC/OSIRIS were unaffordably expensive in terms of observing time, and in fact impossible since OSIRIS currently has limited spectroscopic capabilities (only long-slit). We therefore used spectroscopic data taken with other telescopes. In any case, a spectro-photometric standard star was observed with OSIRIS with a grism and each one of our filters, and we checked that our main calibration procedure (described below) is consistent with these (very limited) observations.

For our main calibration procedure, synthetic fluxes were obtained by convolving the spectra for sources distributed all along the FOV with the appropriate transmission curve seen by that source, according to our calibration of the passband (in terms of the position in the FOV, see Section 3.3). The spectra used in this calibration method were taken from two different sources: (1) the *HST* ACS grism data from the PEARS project[21]; and (2) the spectroscopic data released by the Team Keck Treasury Redshift Survey (TKRS; Wirth et al. 2004) and DEEP3 (Cooper et al. 2011) taken with the Keck/DEIMOS instrument. We note that the TKRS and DEEP3 spectra are not flux calibrated; they are not completely flat fielded in the spectral direction (see below), and are subject to the effect of strong sky emission lines and telluric absorption bands in certain spectral regions. For these reasons, our primary calibrator was the PEARS data set of *HST*/ACS spectra. The Keck spectra were used as a consistency check for the primary calibration. In addition, we performed another test of the calibration based on synthetic magnitudes obtained from stellar population models fitting the broad-band photometry for the galaxies with a published spectroscopic redshift and compiled in the Rainbow Cosmological Surveys database (see Pérez-González et al. 2008; Barro et al. 2011a, 2011b). A finer calibration will be carried out in the future based on high signal-to-noise (S/N > 10) spectra for bright objects which are currently being obtained at TNG and the CAHA 3.5 m telescope. The various methods to calibrate the data are explained in the following sub-sections.

3.4.1. Primary Calibrator: HST/ACS Grism Spectroscopic Data

The photometric calibration procedure starts with a crude determination of the zero point based on the comparison of photometry in the SHARDS images with *R*- or *I*-band fluxes. This comparison provides a first estimation of the conversion from counts to AB magnitudes (one single value for a given image). Then, we use the *HST*/ACS spectra to improve this calibration and check the dependence on the position along the FOV. We start by scaling the ACS spectra to the broad-band photometry in the viz bands from the ACS. The rms of the comparison of broad-band photometry and the synthetic fluxes obtained with the grism spectra is 0.38 mag, i.e., this is the typical accuracy of the spectroscopic data for each galaxy. The flux measurement in the ACS bands is carried out within a large enough aperture that it can be compared with photometry in the SHARDS images with negligible seeing effects and also avoids (as much as possible) contamination from nearby sources. Typically, apertures with radii larger than 1″ were used. The basics of the procedure are outlined in Figure 4: the spectra are scaled to the broad-band photometry, we measure the flux in the SHARDS passband corresponding to the position of the galaxy in the FOV by convolving the spectra with the appropriate transmission curve, and we compare with the flux in counts measured in the SHARDS image, obtaining a conversion from counts to flux densities or AB magnitudes as a function of position in the FOV.

Figure 5 shows the results of the calibration based on *HST*/ACS spectra. We plot the offset between the calibration obtained from the analysis of the *HST* spectra and the preliminary calibration obtained with the comparison with *R*-band fluxes as a function of the CWL of the passband seen by each galaxy. In this example, we show the results for the observations of one of the SHARDS pointings through the F636W17 filter, where we have more than 1,500 ACS spectra to compare with. For the second pointing, PEARS only covered a part of it, and the number of available ACS spectra is ∼900. The derived differential calibration as a function of wavelength (i.e., position) was applied to the images, so the final mosaics have a constant zero point throughout the whole image. The typical scatter around the average calibration was below 0.1 mag. Note that many spectra provided very large zero point offsets. We visually inspected all spectra with offsets above 0.5 mag and virtually all of them showed nearby bright objects which were most probably contaminating the spectra (e.g., the last source

[21] Downloaded from the database at http://archive.stsci.edu/prepds/pears/. See also Ferreras et al. (2009).

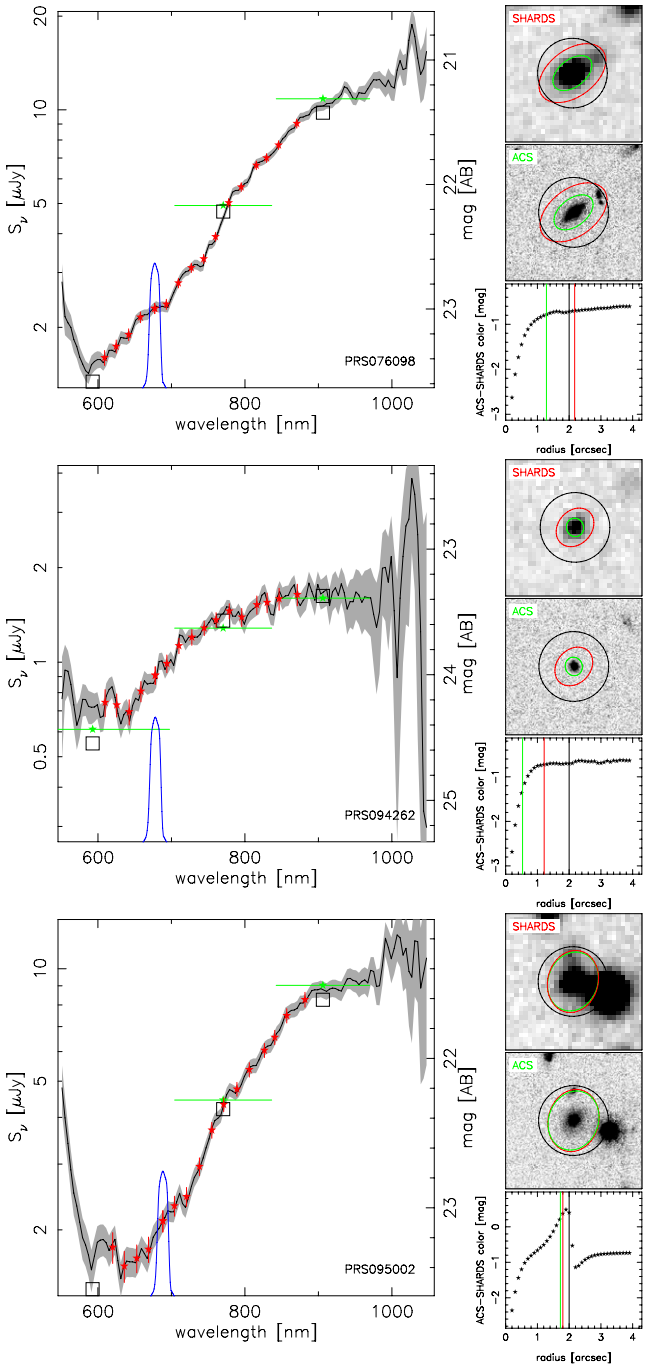

Figure 4. Examples of the *HST*/ACS spectra (from the PEARS data described in Ferreras et al. 2009 and the PEARS database) used in the calibration of the SHARDS data. The ACS spectra are shown in black with the gray shaded area depicting the uncertainties. The spectra are scaled to the ACS viz photometry, shown in green, including also uncertainties and filter widths. The convolutions of the spectra with the viz filter transmission curves are shown with squares. The passband for the F687W17 filter seen by each galaxy is shown in blue, and the convolution with the *HST* spectra is marked with a red star, along with the convolutions for the other SHARDS filters observed so far (no transmission curves are depicted for the sake of clarity). We show the SHARDS and *i*-band ACS images of the galaxy ($5'' \times 5''$) and the color between them as a function of aperture radius. In each plot, the best elliptical aperture determined by SExtractor (Bertin & Arnouts 1996) for the ACS data is shown in green, the best aperture for the SHARDS image is plotted in red, and the circular aperture used to calibrate the SHARDS data is shown in black. The panel in the last row shows a galaxy whose photometry (and probably spectra) is affected by contamination from nearby sources. This kind of source was excluded from our calibration procedure. They are marked with gray symbols in Figure 5.

(A color version of this figure is available in the online journal.)

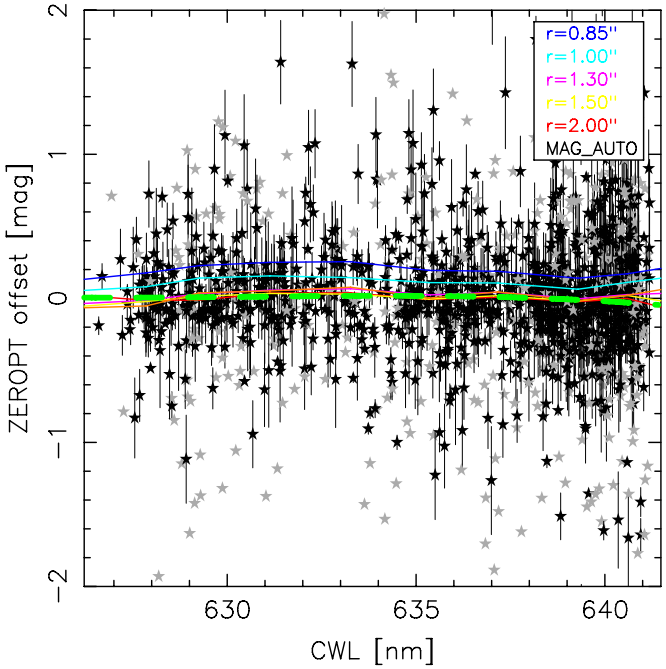

Figure 5. Calibration of the SHARDS data for filter F636W17 based on the *HST*/ACS spectra. The difference between the AB magnitude obtained from the spectra and the magnitude measured in the SHARDS images is plotted as a function of CWL of the passband seen by the galaxy (i.e., vs. position in the FOV, as described in Section 3.3 and defined by Equation (1)). The points show the calibration obtained from individual galaxies for the best photometric aperture, i.e., that enclosing the entire object and minimizing the uncertainties, the effects of seeing, and the contamination from close neighbors. Error bars are estimated from the grism flux uncertainties and the rms of the comparison of ACS spectra and broad-band photometry in the $bviz$ filters (0.4 mag). Objects whose photometry is affected by nearby sources, or that have low-S/N spectra, are plotted with gray symbols. Colored solid lines show the median behavior for the offset calculated with different photometric aperture radii. The final calibration is shown with a green dashed line, resulting from a polynomial fit to the best aperture data.

(A color version of this figure is available in the online journal.)

in Figure 4). This effect was confirmed by comparing the scale factor of the spectra to the broad-band photometry. In spectra affected by contamination by nearby objects, the three bands used in the scaling provided very different factors, with the scatter being considerably larger than the typical value (∼0.4 mag). Note also that we did not establish any magnitude cut in the *HST*/ACS data, and a significant fraction of the spectra corresponded to very faint objects and counted with large uncertainties.

3.4.2. Calibration Test: Ground-based Spectroscopic Data

The calibration obtained with the *HST* data was checked with other spectra taken from the literature. We found nearly 1,000 spectra for sources detected by SHARDS in the TKRS database and the DEEP3 release in GOODS-N (Wirth et al. 2004; Cooper et al. 2011). The spectra were all taken with the DEIMOS instrument on Keck with typical exposure times of 1–2 hr through $R \sim 300$–600 grisms. Given that these surveys were mainly interested in spectroscopic redshifts based on emission lines, the typical S/N in the continuum is low (S/N ∼ 1 per pixel at the original spectral resolution). In addition, the spectra are not flux calibrated and they typically show a decrease of flux to the blue that seems to arise from the lack of an accurate spectral flat correction (see Figure 6). Moreover, these spectra were taken through a mask with slit widths of $1''$, so aperture effects may

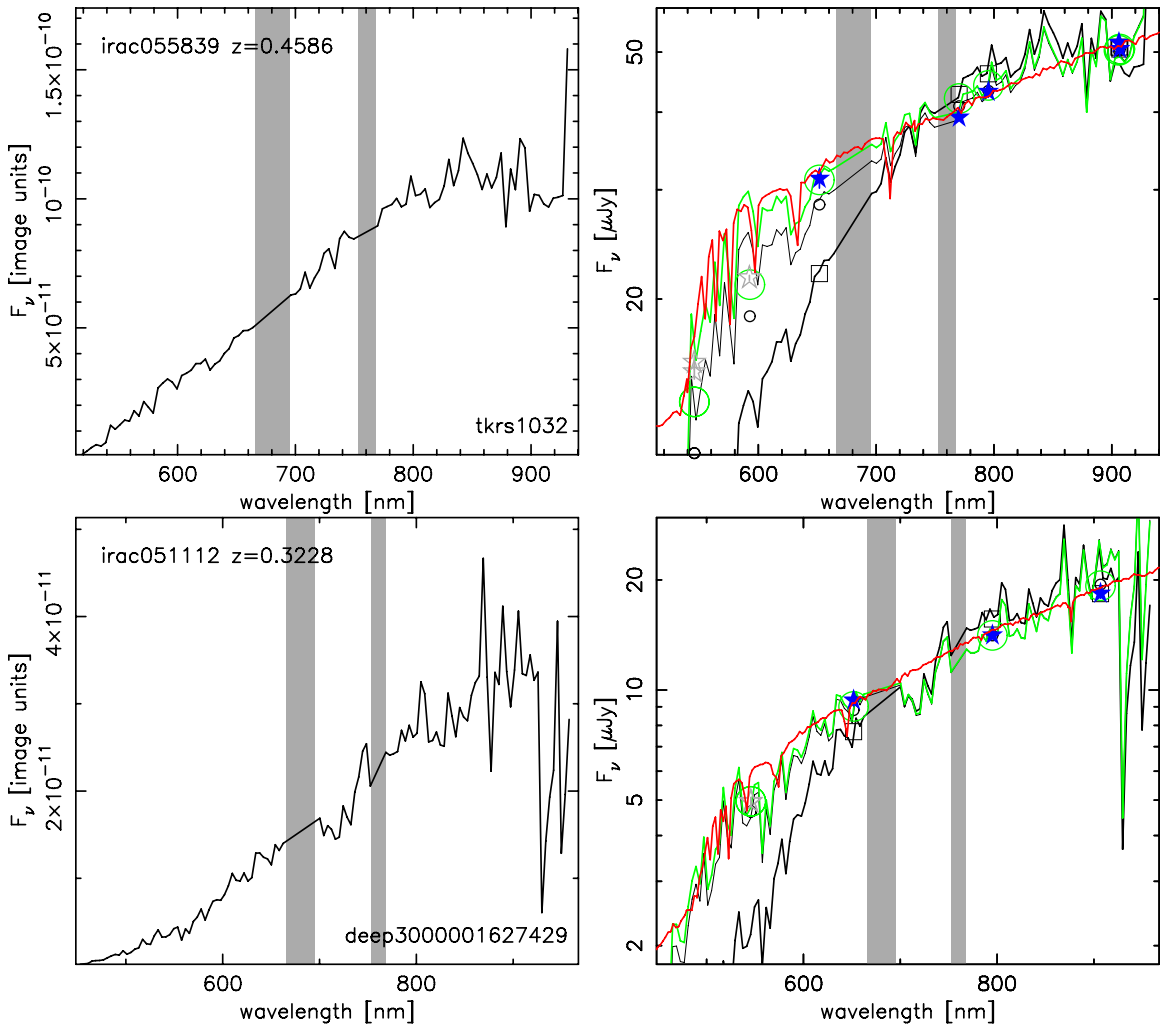

Figure 6. Two examples of the ground-based spectra used to test the absolute flux calibration of the SHARDS data. For each galaxy, the original spectrum (in arbitrary F_ν units and binned to achieve a resolution of 2 nm) is plotted on the left, indicating the name of the source in the Rainbow Cosmological Surveys database (Pérez-González et al. 2008), the TKRS and DEEP3 catalogs (Wirth et al. 2004; Cooper et al. 2011) and the spectroscopic redshift. Both on the left and right panels, we mark with a shaded area the regions where strong telluric absorption bands are located. On the right, we show with a black thick line the original spectrum after flux scaling it to match the broad-band photometry, depicted with blue stars (only the reddest points were used in this first scaling, given that they provided a better absolute calibration) and gray symbols (for the bluest bands which are more affected by the spectral flat and atmospheric extinction corrections). The thin black line shows the same spectrum after applying an average spectral flat obtained as explained in the text. The green line shows the final ground-based spectrum used for the calibration of SHARDS data, obtained after applying an atmospheric extinction correction calculated through a comparison with a stellar population synthesis model fitting the broad-band photometric data, shown in red in the plots. Black squares and circles, and green circles show the convolution of the previously described spectra (respectively, the original after flux calibration, the one after further calibration with a spectral flat fielding, and the final one after also carrying out an extinction correction) with the transmission curves for the broad-band filters.

(A color version of this figure is available in the online journal.)

also be significant, i.e., the spectroscopic data give information about the central part of the galaxies and a comparison with seeing-limited photometry can be biased. For these reasons, we just used these spectra as a test for our basic absolute flux calibration based on *HST* data. Prior to this test, we had to correct the individual ground-based spectra with an average spectral flat and flux calibrate them. Both procedures were carried out using broad-band data and fits to this photometry with SPS models from the Rainbow Cosmological Surveys database (Pérez-González et al. 2008).

Figure 6 shows two typical spectra in GOODS-N extracted from the ground-based spectroscopic sample. After binning the spectrum to a resolution of 2 nm, we carried out a preliminary flux calibration of the spectrum based on the photometric broad-band data around 800 nm (blue stars in the right panels of the figure). An inspection of the resulting calibrated spectra (thick black lines in Figure 6) revealed that the spectroscopic data were not corrected with an adequate spectral flat, resulting in a large and increasing flux difference between the spectra and the broad-band photometric data at shorter wavelengths (see the comparison between the thick black lines and the photometry in Figure 6). To correct for this effect, we built a master spectral flat by averaging the ratio between the spectra and SPS models fitting the broad-band photometry (red lines in Figure 6) for all sources in the spectroscopic sample. After applying this correction, the comparison between the spectra (thin black lines in Figure 6) and the photometry was better, but still most sources showed a dimmer flux level in the spectra when compared with the photometry for the bluest wavelengths. We identified this flux difference as an effect of differential extinction, which was not fully taken into account in the average spectral flat. To account for this, we applied a final correction based on a typical extinction curve at Mauna Kea scaled to explain the difference between the spectra and the broad-band photometry (especially

in the bluest bands). This final spectrum (green lines in Figure 6) was then convolved with the SHARDS filter passband (the appropriate one according to the position of the galaxy in the FOV), providing another independent calibration for our data.

3.4.3. Calibration Test: Synthetic Photometry

Finally, the fluxes obtained in the SHARDS bands were compared directly with synthetic magnitudes obtained by convolving the SHARDS filter passbands with SPS models fitting the broad-band photometry for each source. Note that this calibration test is not completely independent of that carried out with the ground-based spectra since those spectra were partially calibrated with the stellar population fits. Moreover, the comparison with models for individual galaxies may be biased due to the presence of emission lines, which are not constrained by the broad-band photometry. However, because of the lower noise of the templates, we can compare them with a large number of galaxies. Moreover, even the fits for galaxies with no spectroscopic redshift could be reliable in a statistical way because our convolutions with the SHARDS filters are interpolations between broad-band fluxes. Therefore, the comparison with the templates is another good test of the absolute flux calibration, and it indeed provided reassuring results for all filters.

In summary, the flux calibration of the SHARDS data was primarily based on the comparison with *HST*/ACS grism spectra. This calibration was tested through a comparison with ground-based spectra and SPS models fitting the broad-band photometry. Based on these three different calibrators, we also estimated the typical uncertainty in the zero points of the SHARDS images, typically 0.05–0.08 mag (given in Table 1).

3.5. Data Quality

The SHARDS data presented in this paper were obtained in queue mode, and a maximum seeing threshold was set to 0.″9. This image quality was imposed in order to reach the flux limits necessary to detect and reliably measure absorption indices for massive quiescent galaxies up to $z \sim 2.5$ (26.5–27.0 mag at the 3σ level). In Table 1, we show the final seeing of the SHARDS images, measured after mosaicking all the data for a given filter and carrying out all reduction and calibration steps. Virtually all SHARDS data were taken under sub-arcsec conditions.

Concerning the final depth of our images, we give in Table 1 the typical depths reached at the 3σ level (measured in SExtractor-based mag_auto apertures), and the magnitude level corresponding to the third quartile of the brightness distribution. The desired depths were reached in most of the filters, with some of them presenting exceptional seeing and depth figures.

4. SHARDS SCIENCE VERIFICATION: EMISSION-LINE GALAXIES

The analysis of emission lines in the spectra of star-forming galaxies (SFGs) and objects hosting active galactic nuclei (AGNs) is one of the main tools for understanding galaxy evolution. Emission lines can be used to select both SFGs and AGNs, and then to obtain estimations of relevant physical parameters, redshift, SFR, metallicity, or black hole mass being some of the most interesting (see, e.g., Charlot & Longhetti 2001; Kewley & Dopita 2002; Gilbank et al. 2010; Yates et al. 2012).

Although the most straightforward way of obtaining emission-line identifications and fluxes is through spectroscopic observations, these data are hard to obtain for a large number of objects, and acquiring them is very time consuming. Moreover, current spectrographs on the largest telescopes are only able to reach continuum magnitudes around $RI \sim 24$–25 mag. This results in a scarcity of spectroscopic data for faint objects, especially at $z \gtrsim 1.5$, and a bias of spectroscopic surveys toward bright emission-line galaxies (ELGs) at $z \lesssim 1$.

A powerful alternative to spectroscopic surveys can be found in (ultra-)deep narrow-band imaging observations, which have been demonstrated to be useful in selecting ELGs with the faintest magnitudes, and measuring important quantities such as equivalent widths (EWs) and line fluxes (see Teplitz et al. 1998; Kodaira et al. 2003; Pascual et al. 2001; Ouchi et al. 2004; Willis & Courbin 2005; Ly et al. 2007, 2011; Takahashi et al. 2007; Villar et al. 2008, 2011; Shioya et al. 2008; Nilsson et al. 2009; Sobral et al. 2009; Guaita et al. 2010; Hayes et al. 2010a). In addition, although imaging data cannot directly provide robust identifications and precise observed wavelengths for emission lines, they certainly help determine accurate photometric redshifts, even for very high redshift sources, based on the detection of both emission features and absorption bands or breaks.

4.1. ELGs at Intermediate Redshift

In this section, we analyze the sensitivity and spectral resolution of our ultra-deep medium-band survey to select ELGs and measure their relevant parameters (EW, flux). Imaging surveys in the optical aimed at selecting ELGs usually employ narrow-band filters, with narrow meaning widths around 10 nm. The SHARDS filters are wider; the typical FWHM is 15 nm, but the depth, photometric accuracy, and imaging quality of the GTC data (see Table 1) can compensate for the lower spectral resolution ($R \sim 50$), compared to more classical narrow-band surveys.

Figure 7 shows an example of the selection of ELGs with SHARDS data for one of our 24 filters, centered at 687 nm (filter F687W17). The method is similar to that used by narrow-band surveys such as the ones referenced above: the flux in a given photometric band at wavelength $\lambda_{\rm line}$ is compared with the average flux around that wavelength. Sources with emission lines lying inside the central filter would present an excess of flux compared to the average around it, with the latter corresponding to the spectrum continuum next to the line. In this particular example, we would expect to identify a population of galaxies at $z \sim 0.80$–0.84 featuring an excess in the flux seen by the F687W17 filter due to [O II] emission. Note that the redshift interval is governed by the width of the filter as well as by the CWL variation of the passband along the FOV. Other lines could provide samples at different redshifts selected with the same F687W17 filter (e.g., Lyα at $z \sim 4.6$).

Typical narrow-band surveys use a broad-band filter to determine the continuum (e.g., Villar et al. 2008; Takahashi et al. 2007; Sobral et al. 2009, 2012; Hayes et al. 2010b), or one or several narrow- or medium-band filters around a given one (Lee et al. 2012). In our case, the contiguous spectral coverage of the optical window allows us to obtain a continuum determination by using the filters adjacent to a given one, or even several filters around the central passband. This measurement is very robust, since it takes into account the intrinsic color of each galaxy in a close region around the spectral region of interest, rather than providing an average continuum value in a wide wavelength range. Moreover, the continuum determination is not affected by the emission line itself (for a typical line such as [O II] λ3727), as would be the case for surveys using broad-band filters.

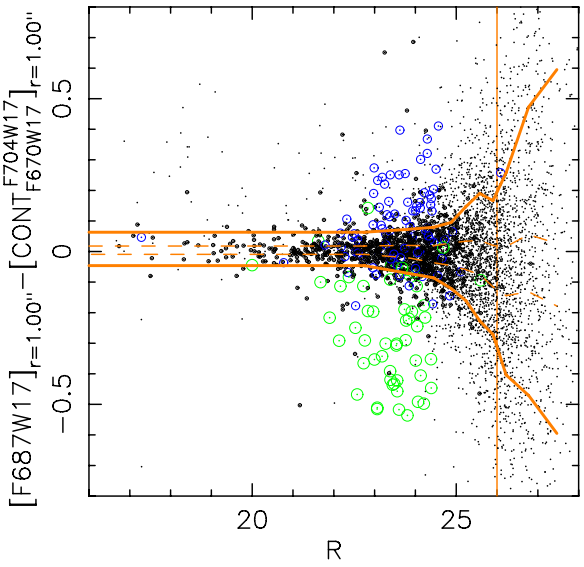

Figure 7. Color–magnitude diagram showing ELG candidates at ∼687 nm in SHARDS pointing 1. The vertical axis shows the color between the F687W17 band and the average magnitude in the adjacent SHARDS bands (F670W17 and F704W17) measured within a circular aperture of radius $r = 1''$. Sources with measured spectroscopic redshifts implying that the [O II] line lies within the F687W17 filter are marked in green, while sources whose [O II] emission is located in the adjacent filters are marked in blue. Solid points show galaxies with a photo-z between $0.7 < z < 0.9$. The dashed orange lines depict the typical photometric uncertainty as a function of magnitude. The locus for ELGs with an emission line within the F687W17 filter detected with more than 3σ confidence is the region below the bottom orange continuous line. ELGs with emission lines within the F670W17 or F704W17 passbands should be located above the top orange continuous line. The vertical orange line shows the 5σ detection threshold of the SHARDS survey in the F687W17 band. Only the sources detected by IRAC for which robust photometric redshifts were estimated (Pérez-González et al. 2008) are depicted.

(A color version of this figure is available in the online journal.)

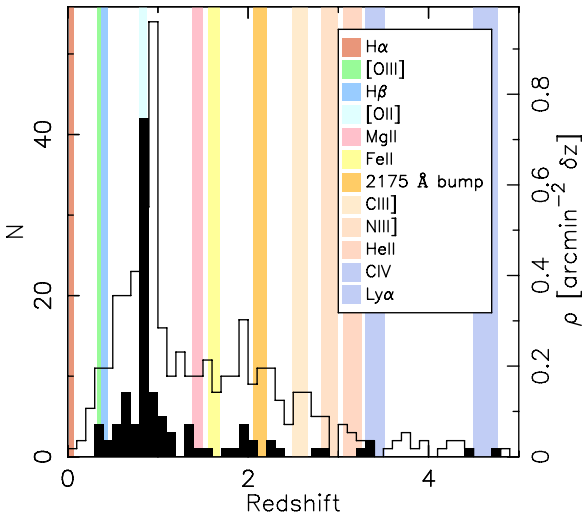

Figure 8. Spectroscopic and photometric redshift distributions of the sources selected as ELGs with the F687W17 filter for pointing 1. The filled histogram shows the selected galaxies with spectroscopic redshifts. The open histogram shows all ELG candidates using photometric redshifts (Pérez-González et al. 2008). The expected redshifts for emitters with some of the most typical lines (e.g., Lyα, [O II], [O III], or Hα) are marked as shadowed regions. We also mark spectral features such as the Mg–Fe absorption band at ∼280 nm, or the 2175 Å dust absorption bump (which would imprint an absorption in the galaxy SED).

(A color version of this figure is available in the online journal.)

In order to understand the scatter in Figure 7, we have analyzed the photometric uncertainties of our catalogs. The distribution of the typical errors of our data is shown with dashed lines. Sources whose emission in the F687W17 filter is brighter than the average for the adjacent filters with more than the 3σ confidence are located below the continuous orange line. This is the expected locus for ELGs. Note that the color to detect a line with medium-band filters such as ours ranges between 0.1 and 0.5 mag, approximately. For filters with larger widths (e.g., broad-band), emission lines such as the ones we are able to detect would be diluted by the ratio between filter widths, and thus would be very hard to detect with broad-band data (typically having widths a factor of 7–8 larger than the SHARDS filters, implying an effect on the broad-band photometry of less than 0.1 mag for the brightest lines).

In order to test how the SHARDS data perform when trying to select ELGs, we have marked in Figure 7 with green symbols the galaxies with reliable spectroscopic redshifts for which the [O II] line would lie within the F687W17 passband.[22] We are able to recover more than 90% of the spectroscopically confirmed galaxies with an [O II] emission-line expected within the F687W17 filter. A visual inspection of the spectra for the non-selected objects (but with $z \sim 0.8$) revealed very weak or even absent [O II] emission lines. Therefore, we conclude that the SHARDS data are very effective in isolating emission-line galaxies at a similar line flux level as deep spectroscopy.

It is also interesting to note that virtually all the spectroscopically confirmed ELGs in Figure 7 are brighter than $R \sim 24.5$. This is the spectroscopic limit of the redshift surveys carried out in the GOODS-N field, and the typical detection threshold for the vast majority of data taken with state-of-the art spectrographs in 10 m class telescopes. The SHARDS observations reach at least 2 mag fainter, and thus open the possibility to reliably select and study fainter and/or higher redshift ELGs.

Figure 8 shows the redshift distribution of the sources selected as ELGs by SHARDS with the F687W17 filter. The filled histogram represents galaxies with spectroscopic redshifts, i.e., confirmed ELGs. The open histogram shows the photometric redshifts (Pérez-González et al. 2008) for all ELG candidates. These redshift distributions demonstrate that the ELGs selected by SHARDS are preferentially located in the appropriate redshifts corresponding to the most common emission lines detected in intermediate- and high-redshift galaxies. The majority of the selected sample are [O II] emitters at $z \sim 0.8$.

Our observational strategy was conceived to detect and measure absorption bands. In this regard, absorption features such as the Mg+Fe absorption band (at ∼280 nm), the Balmer and 4000 Å breaks, or the dust absorption peak at 2175 Å shown in certain extinction laws (such as the Milky Way's; Cardelli et al. 1989), can mimic an emission line in a color–magnitude diagram such as the one depicted in Figure 7 (see also Figure 9).

Figure 9 shows eight examples of galaxies selected by SHARDS as emission-line sources and counting with spectroscopic confirmation (shown in green in Figure 7). These sources have been selected using the F687W17 filter as central band. The two sources on the top row are examples of low-redshift galaxies detected because of their [O III] λλ4959, 5007 emission (forming the peak at $z \sim 0.3$ seen in Figure 8 and marked in blue and green). We compare our spectro-photometric data with the available Keck and *HST*/ACS grism spectroscopy. Unlike the

[22] Note that these galaxies have been highlighted only because of their redshift, i.e., some of them may not show [O II] emission, their spectroscopic redshifts being based on some other spectral feature.

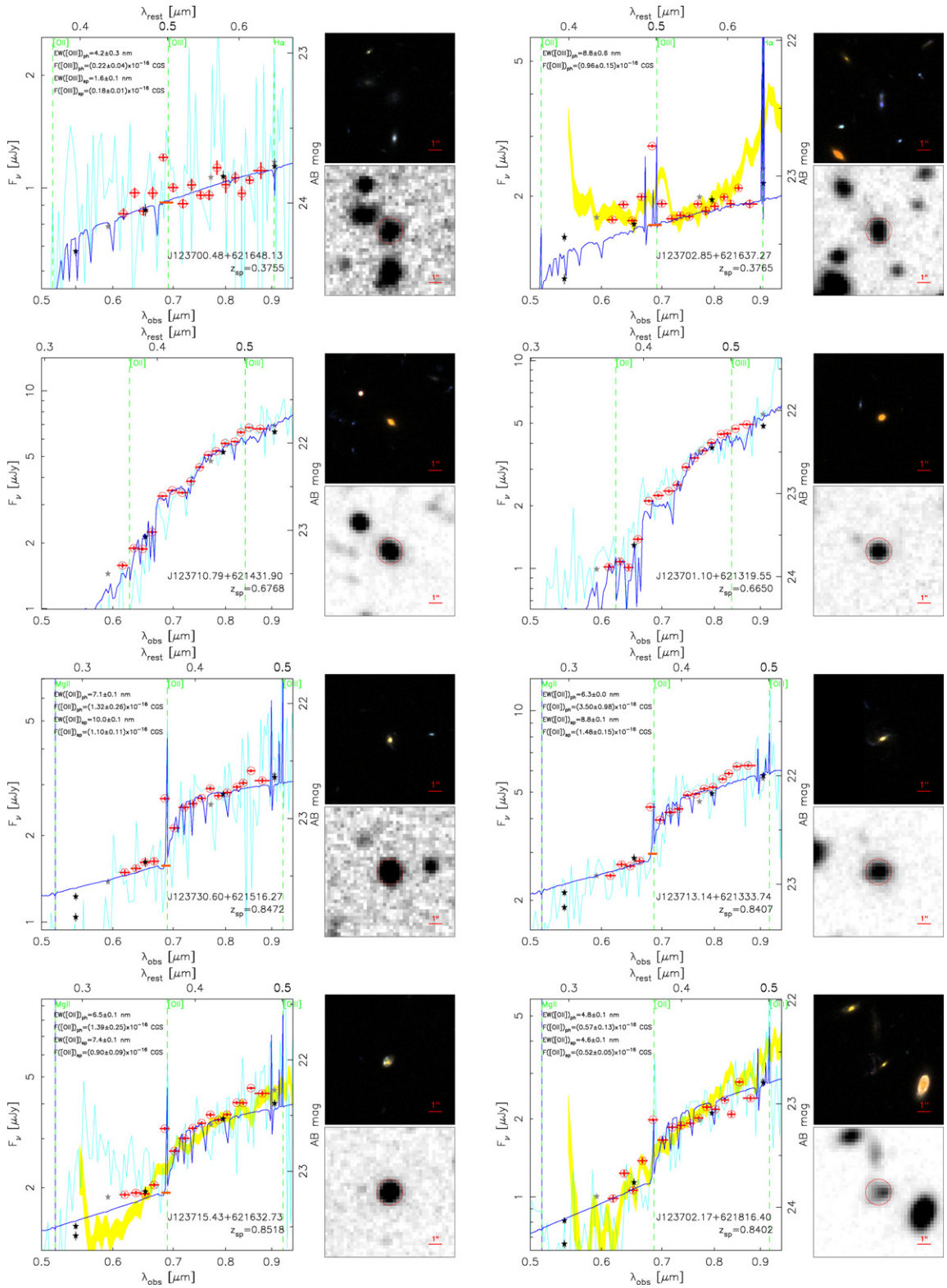

Figure 9. SEDs and postage stamp images of some representative examples of the ELG candidates selected with the SHARDS F687W17 filter (from Figure 7). We show galaxies which have already been spectroscopically confirmed. On the left panel for each galaxy, we depict the optical SED of the source. Broad-band photometric fluxes are depicted with black (ground-based) and gray (*HST*) filled stars. Red symbols show the SHARDS data, including uncertainties and filter widths. Blue lines represent SPS models fitting the broad-band data, which were used to obtain an estimation of the photometric redshift and stellar mass (Pérez-González et al. 2008). The cyan lines show ground-based spectra for each source, when available; the spectral and absolute flux calibration explained in Section 3.1 have been applied. For some sources, we also depict with a yellow shaded area the available *HST*/ACS grism spectrum from PEARS (including uncertainties). The wavelength for several typical emission lines are marked in green. We also give measurements of EWs and fluxes for the [O II] and [O III] lines when they lie within the F687W17 filter passband, using both the spectroscopic and the photometric SHARDS data. On the right for each galaxy, we show postage stamp images in the ACS bands (RGB image on top) and the SHARDS F687W17 filter (bottom). North is up and east is left; image sizes are $10'' \times 10''$, and the ELG confirmed candidate is marked with a red circle (radius $1''$).

(A color version of this figure is available in the online journal.)

noisy spectra, our data allow us to study the continuum (compare with the SPS models shown in blue, which were fitted to the broad-band data; see Pérez-González et al. 2008). Using all the SHARDS photometric data points and fitting them to stellar population models, we have estimated this continuum level and, combining this with the flux measurement for the F687W17 filter, we have obtained line fluxes and EWs. Note that our method to estimate the continuum is not based on the bands adjacent to that containing the emission line alone, but on a stellar population model fit to all bands (except that containing the line). When comparing to the values obtained from the spectroscopy, we typically find smaller EWs. We interpret this systematic difference as an aperture effect, given that our photometric apertures are typically 1.″0–1.″5 in radius, probably larger than the typical slit widths and extraction sizes used in spectroscopic surveys. Note that larger apertures would easily dilute the emission lines in a brighter continuum, thus resulting in smaller measurements of the EW. We will present a detailed analysis of the comparison between fluxes obtained with photometry and spectroscopy in a forthcoming paper (A. Cava et al. 2012, in preparation).

On the second row of Figure 9, we show two examples of galaxies located in the ELG locus in Figure 7, but not showing emission lines. These sources were selected due to the significant flux difference between adjacent bands around the 687 nm filter. In this case, this large color is due to the presence of the Balmer or 4000 Å break at approximately 680 nm (as clearly shown by the available ground-based spectra and SPS models). These Balmer break/D(4000) sources form the peak at $z \sim 0.7$ and the redshift tail between the $z \sim 0.8$ peak, which corresponds to [O II] emitters, and $z \sim 1.2$ seen in the redshift histogram in Figure 8. The postage stamp images show that these sources are typically red spheroids, where strong 4000 Å breaks are expected. Again, our SHARDS data are able to probe this spectral region with high accuracy and measure absorption indices such as the D(4000). We refer the reader to Section 5 for a discussion on the detection of absorption features with SHARDS data and their use for SPS models.

The third and fourth rows in Figure 9 show [O II] emitters with spectroscopic confirmation (from Keck and *HST* grism data) selected in the F687W17 band ([O II] around $z = 0.8$). These examples clearly demonstrate that SHARDS data are able to detect faint ELGs, which may even be missed by low-resolution spectroscopy such as that from *HST*/ACS grism data. This is the case for the sources in the bottom row, whose [O II] emission is not measurable with *HST*/ACS data, but was confirmed with ground-based medium-resolution spectroscopy. We would also like to highlight that our medium-band spectro-photometric data are able to detect and robustly measure emission lines as faint as $\sim 5 \times 10^{-17}$ erg s^{-1} cm^{-2}.

Finally, we also point out that the postage stamp images shown in Figure 9 demonstrate the depth and excellent image quality of the SHARDS images, which are able to detect the majority of the faint objects seen in the ACS data.

In summary, our science verification test has demonstrated that SHARDS is able to detect virtually all the spectroscopically confirmed ELGs at intermediate redshift. This opens the possibility to extend and attain higher completeness in the samples of ELGs in GOODS-N, and to carry out a comprehensive analysis of SFGs and AGNs down to fainter magnitudes (∼26.5 mag) than spectroscopic surveys. A complete analysis of the properties of the ELGs detected by SHARDS will be presented in a forthcoming paper (A. Cava et al. 2012, in preparation).

4.2. ELGs at Very High z

The ultra-deep imaging data from SHARDS could, in principle, allow us to detect and study sources at very high z ($z \gtrsim 3$). Indeed, reaching magnitudes as faint as 26.5–27.0 mag in all bands from 500 to 941 nm is deep enough to detect interesting sources such as Lyα emitters (LAEs) at $z > 3$ and up to $z \sim 6.7$ (Kashikawa et al. 2006; Bouwens et al. 2006; Ouchi et al. 2003, 2008). In Figure 10, we show one example of a spectroscopically confirmed AGN at $z > 3$ where SHARDS data reveal the presence of several emission lines such as C III] λ1909 or C IV λ1548. The SED of this AGN shows that the spectro-photometric data from SHARDS is completely consistent and provides a similar spectral resolution to the *HST* grism data from PEARS. Our data can be used to obtain very robust fluxes and flux densities for both emission lines and the continuum for a source which is as faint as the typical spectroscopic limit of ground-based state-of-the-art spectrographs in 10 m class telescopes (see the noisy Keck spectrum for this source). Note that SHARDS data are not yet available at wavelengths below ∼600 nm, but when our survey is complete we should be able to detect and measure fluxes for Lyα in this kind of object (AGNs or star-forming galaxies).

A preliminary analysis of the SHARDS data in four filters from 687 to 738 nm revealed a dozen dropout sources (in one of the four filters) with SEDs consistent with $z > 4$ LAEs and LBGs. Figure 10 shows one of these LAE candidates at $z \sim 5$, including postage stamps and an SED. In fact, the postage stamps show two LAE candidates, both appearing in the F738W17 filter (one of them being almost undetected in the ACS bands). The galaxy shown in the SED is a dropout in the F721W17 filter. Its emission is booming in the F738W17 filter, and then becomes fainter again (but detected) in redder filters. This points to a Lyman break located within the two mentioned SHARDS filters, which would imply a redshift around $z = 5$. This figure demonstrates the potential of the SHARDS ultra-deep medium-band survey to select magnitude 26–27 ELGs at very high redshifts. We refer the reader to J. M. Rodriguez-Espinosa et al. (2012, in preparation; see Rodriguez-Espinosa et al. 2012) for a more detailed discussion on the detection and properties of the LAEs detected by SHARDS.

5. SHARDS SCIENCE VERIFICATION: ABSORPTION SYSTEMS

The main goal of the SHARDS project is to analyze in detail the stellar populations in massive galaxies at high redshift, especially those that are already evolving passively. The observational strategy of the survey was devised to be able to construct rest-frame UV/optical SEDs for this kind of source with enough spectral resolution to measure absorption indices correlated with important physical parameters such as the age of the stellar populations.

The main absorption index targeted by SHARDS for high-z passively evolving sources is the Mg index, $\mathrm{Mg_{UV}}$. This index probes several absorption lines (e.g., Mg I λ2852, Mg II λλ2796,2804, Fe II λλ2600, 2606) and has been shown to be an extremely reliable means of detecting quiescent massive galaxies. In addition, the absorption lines can be used to easily distinguish the SED of a quiescent massive galaxy from the featureless spectrum of a dusty starburst (Daddi et al. 2005a). The relative intensity of these absorptions can be measured with the $\mathrm{Mg_{UV}}$ spectral index, directly linked to the age of the stellar population (e.g., Bruzual & Charlot 1993). The index is easily and robustly

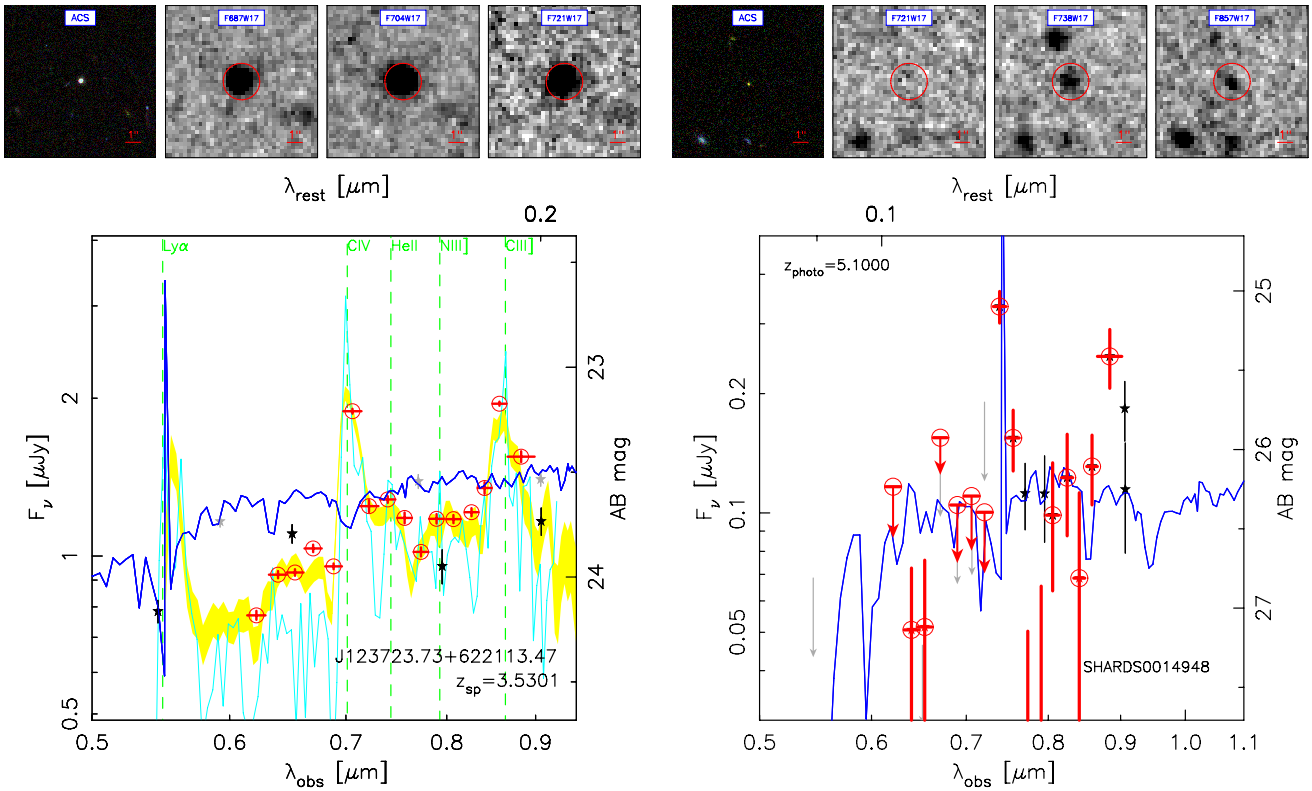

Figure 10. Examples of SEDs constructed with SHARDS data for $z > 3$ galaxies. Symbols and lines are as in Figure 9. For each source, postage stamp images in several bands are also given. On the left, we show a spectroscopically confirmed AGN at $z \sim 3.5$ for which the SHARDS spectro-photometric data provide clear detections of emission lines such as C III] and C IV. On the right, we show a dropout source which has been selected as a candidate for an LAE at $z \sim 5$ with a possible companion (also an LAE at the same redshift) to the NE (Rodriguez-Espinosa et al. 2012). The SHARDS data (and the very few detections in broad-band imaging observations) are fitted with an SPS model that predicts an intense Lyα emission at around 740 nm, corresponding to $z = 5.1$.

(A color version of this figure is available in the online journal.)

measurable even in low-resolution spectra ($R < 100$; Daddi et al. 2005a). The Mg_{UV} index has been successfully used in the past to obtain redshifts and ages of stellar populations in massive galaxies at high-z (Spinrad et al. 1997; Cimatti et al. 2004; McCarthy et al. 2004; Saracco et al. 2005; Daddi et al. 2005a; Ferreras & Yi 2004; Ferreras et al. 2012).

Other interesting absorption features probed by SHARDS (for galaxies at different redshifts) are the Balmer and 4000 Å breaks, or the Ca HK lines, the G band, and the Mg_1, Mg_2, and TiO_2 molecular bands (among others). All these have been extensively used to study stellar population ages (e.g., Burstein et al. 1984; Worthey 1994; Worthey et al. 1994; Balogh et al. 1999; Lotz et al. 2000; Franx et al. 2003; Kauffmann et al. 2003b; Förster Schreiber et al. 2004; Gallazzi et al. 2005; Kriek et al. 2006, 2011; Muzzin et al. 2012, see also the review by Renzini 2006). The spectral resolution of the SHARDS data set is adequate for measuring the Balmer or $D(4000)$ breaks with high accuracy. For galaxies with spectroscopic redshifts or very accurate photometric redshift (errors below 1%), we have very similar accuracies to those achieved in standard spectroscopic studies of nearby galaxies and synthesis models, which typically use bands of 10–20 nm around the feature (Bruzual 1983). In the case of the molecular bands, the widths of the SHARDS filters are larger than the amplitude of these absorptions, but, given their strength, they should have a measurable effect on the photometry through filters such as ours. In any case, our filters are narrower (by at least a factor×2) than those used by other optical and NIR medium-band surveys (such as MUSYC (Cardamone et al. 2010) or NMBS (Brammer et al. 2009)). This allows us to probe these features with higher resolution. In addition, as demonstrated in the previous section, SHARDS data are also very sensitive to emission lines, so they can be used to detect low level residual (unobscured) star formation in massive galaxies at high-z and confirm their quiescent state (along with other methods, such as the study of the MIR/FIR emission).

5.1. Study of Quiescent Massive Galaxies at High-z

In this section, we demonstrate the power of the SHARDS data set to accurately measure absorption indices and study high-z massive galaxies. To do so, we focus on quiescent massive galaxies with reliable spectroscopic redshifts above $z = 1$. Rather than measuring and studying one specific absorption index, we combine all the photometric information for each source and fit the entire SED with SPS models, i.e., we include SHARDS fluxes and also broad-band data up to the MIR wavelengths probed by *Spitzer*/IRAC. We therefore use all the (photometric) observations available for our sample of quiescent massive galaxies to carry out the most reliable analysis possible of their stellar population properties. We concentrate our study on $z \sim 1$–2, a critical redshift range in which massive quiescent galaxies assembled a significant fraction of their mass (Arnouts et al. 2007; Pérez-González et al. 2008; Ilbert et al. 2010; Nicol et al. 2011; Brammer et al. 2011). In this redshift interval, the $D(4000)$ and/or Mg_{UV} absorption features are probed by the SHARDS data.

The sources compiled for this science demonstration exercise have been extracted from several sources in the literature. The sample includes the following.

1. The three galaxies classified as *red nuggets* whose dynamical masses were studied in Newman et al. (2010) and are covered by our data. All the sources in this paper within our surveyed area were detected in all SHARDS individual filters, but some of Newman et al.'s sources lie outside of our FOV.
2. The four galaxies at $z > 1$ from Ferreras et al. (2009), who concentrated their study of early-type galaxies on intermediate redshift sources, but had a few $z > 1$ galaxies in their sample. Given that the galaxies in this paper count with pseudo-spectroscopic redshifts from *HST* optical grism data, we compared the quoted redshifts with our photometric redshifts (Pérez-González et al. 2008) and only selected the four galaxies with consistent estimations.
3. Finally, we also selected those galaxies with spectroscopic redshifts that, according to their observed optical and NIR colors, qualify as extremely red objects (following the definition in Elston et al. 1988 and Yan et al. 2000), and/or distant red galaxies at $z > 1$ Franx et al. (2003).

In order to avoid dusty starbursts in this study and concentrate only on massive galaxies that are evolving passively, we only considered galaxies undetected in the MIPS 24 μm data, which reach fluxes as low as 30 μJy in GOODS-N (reduction and catalogs described in Pérez-González et al. 2005, 2008). This sets an upper limit of 1–10 $M_{\odot}$ yr^{-1} at $z = 1.0$–1.5. The final sample considered in the following discussion is composed of 27 galaxies at $1.01 < z < 1.43$, with virtually all of them having masses above $10^{10.5}\,M_{\odot}$. Their main properties are given in Table 2. Note that we have only considered galaxies with a spectroscopic redshift, so the sample is highly biased toward low redshift (close to unity, the lower limit of our sample, 75% of the sample is at $z < 1.3$ and the average redshift is $\bar{z} = 1.17$) and not (necessarily) representative of the entire population of massive quiescent galaxies at $z \sim 1$.

5.2. Estimating Stellar Population Properties from SED Synthesis Models

Our goal in this section is to improve the characterization of the stellar populations of quiescent galaxies using the unprecedented spectral resolution and depth provided by the SHARDS photometric observations. Recent results based on data with similar medium-band filters and (low-resolution) grism spectroscopy have already shown the power of probing key spectral features on the SEDs of quiescent galaxies, such as continuum breaks and absorption lines/bands, to place more robust constraints on relevant properties of these galaxies such as the age, stellar mass, or SFH (Ferreras et al. 2009; Whitaker et al. 2010, 2011; van Dokkum & Brammer 2010).

Here we study the stellar properties of a sample of 27 massive quiescent galaxies with spectroscopic redshifts above $z = 1$ by fitting their UV-to-MIR SEDs with SPS models. To calibrate the impact of using the SHARDS data in this exercise, we conduct two kinds of test. First, we show how including the SHARDS medium-band data allows us to decrease those uncertainties in the derived stellar parameters linked to well-known degeneracies (such as age–dust or age–SFH). To do so, we analyze the connection between the photometric uncertainties and the best-fit solutions in the parameter space formed by the relevant stellar properties. Second, we study the different results obtained by fitting the SEDs with different sets of SPS models extracted from several of the most common libraries found in the literature.

We start the analysis of the SEDs of massive quiescent galaxies at $z \sim 1$ by describing the set of libraries, the modeling assumptions, the parameter space, and the statistical approach to the analysis of the different solutions and degeneracies.

The UV-to-MIR SEDs for the sample of 27 massive passively evolving galaxies at $z > 1$ were fitted with SPS models from several of the most common libraries found in the literature. We considered SFHs following general exponential decaying models (τ models) using the predictions from the following codes.

1. The Bruzual & Charlot (2003) models (BC03) with a Chabrier (2003) initial mass function (IMF). This was chosen as our fiducial model (BC03-chab, hereafter). In this section and the following, we discuss the properties of our galaxies as inferred by other models in comparison with those obtained with this library and IMF.
2. The Charlot & Bruzual (2009) models (CB09) with a Kroupa and Chabrier IMFs (CB09-krou and CB09-chab, hereafter). These models are thought to be an improvement over the BC03 library with a better treatment of some evolutionary stages of stars.
3. The Maraston (2005) models (M05) with a Kroupa IMF (M05-krou). These models should also give us information about the effects on the derived parameters of specific stellar evolutionary stages such as the TP-AGB phase.
4. the PEGASE code (Fioc & Rocca-Volmerange 1997, P01), assuming a Kroupa (2001) IMF. These are referred to as P01-krou models.

In all cases, we considered the following mass limits for the IMF: $0.1 < \mathcal{M} < 100\,\mathcal{M}_{\odot}$.

The fitting procedure is explained in detail in Pérez-González et al. (2003, 2008). Briefly, the photometry is compared with the models assuming an exponentially decreasing SFH characterized by a τ parameter which runs from 1 Myr (almost identical to a single stellar population, SSP) to 100 Gyr (almost constant SFH). We run models corresponding to the different discrete values of the metallicity given for each library, which run from $Z_{\odot}/200$ to 2.5 $Z_{\odot}$ for BC03 and CB09 models, $Z_{\odot}/200$ to 5 $Z_{\odot}$ for P01, and $Z_{\odot}/50$ to 2 $Z_{\odot}$ for M05 models. We considered an extinction parameterized with a V-band attenuation, $A(V)$, with values ranging from 0 to 2 mag, and assumed the extinction law of Calzetti et al. (2000). Finally, we probed all ages between 1 Myr and the age of the universe corresponding to the source redshift (up to ~6 Gyr for the closest galaxy) to search for the best-fitting model minimizing a reduced χ^2 maximum-likelihood estimator.

In order to study the uncertainties in the derived parameters and to take into account the possible degeneracies in the solutions, we ran Monte Carlo simulations for each galaxy. The method consisted in randomly varying the photometric data points with a Gaussian distribution of width equal to the photometric uncertainty, and repeating the fit again with all possible models. We ran the code 1000 times and then analyzed the set of solutions. This analysis identified the clusters of solutions with a k-means method. Each cluster was assigned a statistical significance, given by the fraction of the 1000 different solutions belonging to the cluster, i.e., the relative

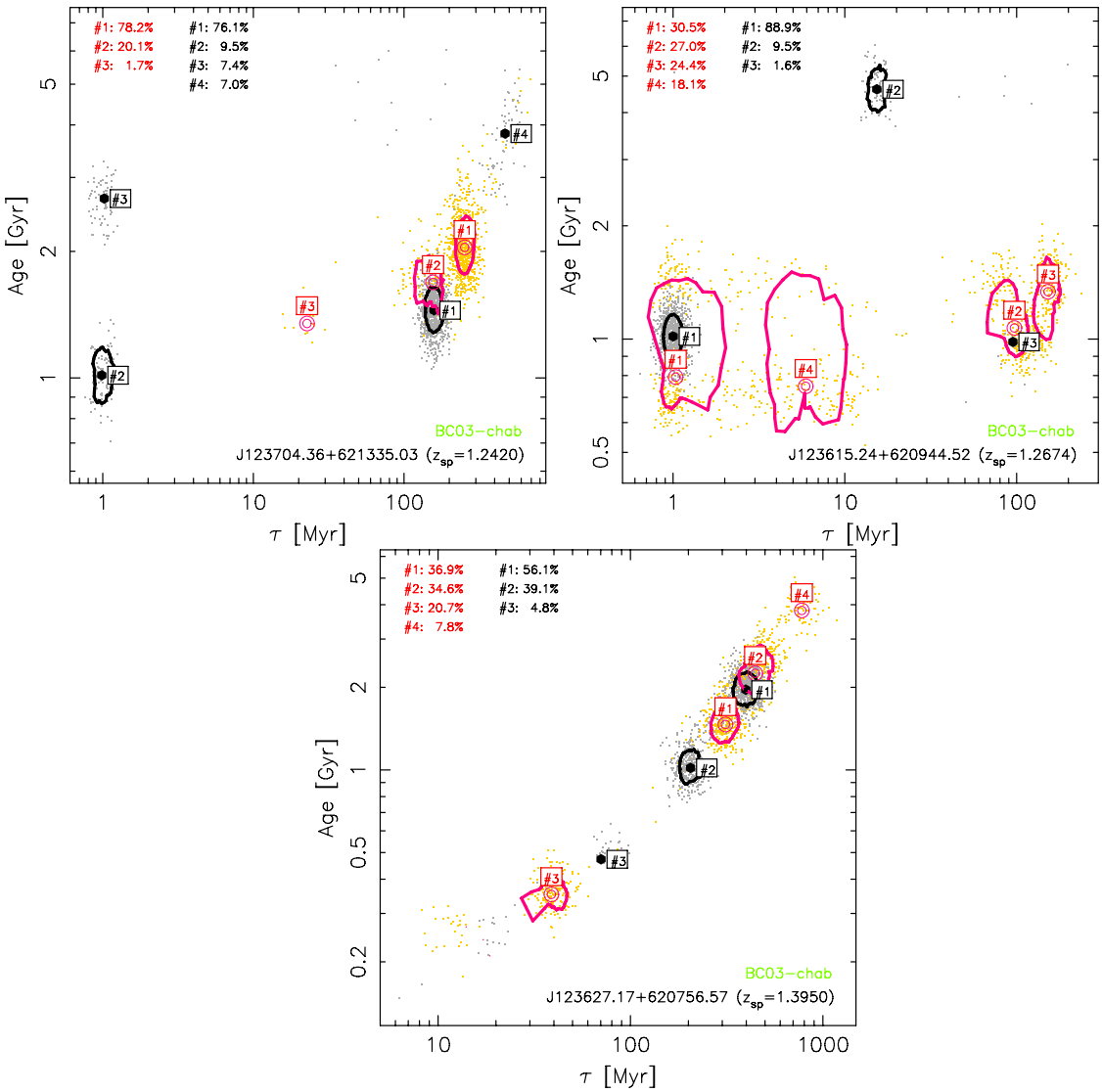

Figure 11. Age and *e*-folding time results for the SPS modeling (using our fiducial library, BC03-chab) of the SEDs of the three massive quiescent galaxies at $z > 1$ presented in Figure 12. For each galaxy, orange points show the solutions when fitting UV-to-MIR broad-band data alone, while gray points show the results when adding the medium-band SHARDS data. Average values for each cluster of solutions are marked with open symbols for the results using broad-band data alone, and filled circles for the solutions also using SHARDS data. Contours show 2σ uncertainties: red for fits to only broad-band, black for fits adding SHARDS fluxes. Statistical significances of each cluster of solutions are also given. Note that the scales are adjusted to each galaxy, but our modeling procedure has probed *e*-folding times from 1 Myr to 100 Gyr, so only a small part of the considered parameter space is shown.

(A color version of this figure is available in the online journal.)

number of solutions which provide similar results and are grouped as a single solution identified by a median value and a scatter in the multi-dimensional space formed by the fitted parameters. Note that we did not use the reduced χ^2 values to assign statistical weights to each cluster of solutions, since χ^2 differences between them are not statistically relevant. Typically, 1–4 clusters of solutions were identified for each galaxy above a statistical significance of 10%. In virtually all cases (all galaxies and models), one solution was dominant with more than 50% of the solution data points belonging to its cluster. Note that different clusters may have different typical reduced χ^2 values, i.e., the data can be better reproduced by some combination of parameters corresponding to one cluster. The different solutions provided information about the typical degeneracies of the study of stellar populations, such as the age–metallicity degeneracy or the one linked to τ (SFH) and age. Table 2 presents the different solutions (the statistically most significant and the secondary solutions) for each galaxy and the statistical weight of each.

5.3. Evaluation of the SPS Modeling with SHARDS Data

In order to test how the spectro-photometric data from SHARDS helps in the SPS modeling of high-z galaxies, we compare in Figure 11 the results obtained when fitting only the broad-band data with those obtained when adding the SHARDS data for three representative galaxies of our sample of quiescent massive galaxies at $z > 1$. The details of the fits and results of the SPS modeling for these galaxies are presented in Figure 12 and Section 5.4.

For the first galaxy, J123704.36 + 621335.03 ($z = 1.2420$), the fits to the broad-band photometry alone provide a dominant solution characterized by an *e*-folding time $\tau \sim 200$ Myr and an age of around 2 Gyr. There is another less statistically significant

Table 2
Stellar Population Synthesis Results for Red and Dead Galaxies at $z \sim 1$

Galaxy (1)	z (2)	Model (3)	τ (4)	Age (5)	$A(V)$ (6)	Z (7)	M (8)	χ^2 (9)	Prob. (10)
J123704.36+621335.03	1.2420	BC03-chab	158^{+18}_{-16}	$1.43^{+0.16}_{-0.13}$	$0.40^{+0.05}_{-0.04}$	$1.000^{+0.000}_{-0.601}$	$10.86^{+0.05}_{-0.04}$	$0.16^{+0.18}_{-0.14}$	76.1
		CB09-chab	32^{+5}_{-5}	$1.02^{+0.10}_{-0.11}$	$0.30^{+0.05}_{-0.04}$	$1.000^{+0.000}_{-0.000}$	$10.69^{+0.05}_{-0.04}$	$0.38^{+0.40}_{-0.35}$	85.6
		CB09-krou	40^{+5}_{-5}	$1.02^{+0.10}_{-0.09}$	$0.40^{+0.05}_{-0.05}$	$1.000^{+0.000}_{-0.000}$	$10.78^{+0.04}_{-0.04}$	$0.37^{+0.39}_{-0.34}$	68.1
		M05-krou	501^{+51}_{-54}	$4.00^{+0.40}_{-0.43}$	$0.20^{+0.05}_{-0.04}$	$0.500^{+0.000}_{-0.000}$	$11.05^{+0.05}_{-0.05}$	$0.22^{+0.25}_{-0.21}$	91.3
		P01-krou	50^{+5}_{-6}	$3.50^{+0.33}_{-0.35}$	$0.50^{+0.05}_{-0.03}$	$0.200^{+0.000}_{-0.000}$	$11.16^{+0.05}_{-0.04}$	$0.28^{+0.30}_{-0.26}$	56.5
		CB09-chab	584^{+94}_{-170}	$4.43^{+0.51}_{-0.18}$	$0.29^{+0.05}_{-0.04}$	$0.200^{+0.000}_{-0.000}$	$11.06^{+0.05}_{-0.05}$	$0.38^{+0.40}_{-0.36}$	14.4
		CB09-krou	494^{+55}_{-58}	$4.72^{+0.45}_{-0.46}$	$0.31^{+0.04}_{-0.06}$	$0.200^{+0.000}_{-0.000}$	$11.16^{+0.04}_{-0.05}$	$0.36^{+0.39}_{-0.34}$	31.9
		P01-krou	347^{+135}_{-45}	$3.77^{+0.61}_{-0.51}$	$0.51^{+0.05}_{-0.06}$	$0.200^{+0.000}_{-0.000}$	$11.13^{+0.05}_{-0.06}$	$0.29^{+0.31}_{-0.27}$	18.2
		P01-krou	227^{+31}_{-42}	$3.07^{+0.56}_{-0.40}$	$0.51^{+0.05}_{-0.05}$	$0.200^{+0.000}_{-0.000}$	$11.10^{+0.06}_{-0.06}$	$0.29^{+0.30}_{-0.26}$	16.9
J123615.24+620944.52	1.2674	BC03-chab	$1.0^{+0.1}_{-0.1}$	$1.02^{+0.10}_{-0.10}$	$1.00^{+0.06}_{-0.05}$	$0.200^{+0.000}_{-0.186}$	$10.95^{+0.05}_{-0.05}$	$0.68^{+0.97}_{-0.46}$	88.9
		CB09-chab	63^{+10}_{-9}	$1.02^{+0.10}_{-0.10}$	$0.20^{+0.05}_{-0.05}$	$1.000^{+0.000}_{-0.000}$	$10.68^{+0.05}_{-0.05}$	$0.83^{+1.16}_{-0.54}$	65.2
		CB09-krou	126^{+16}_{-15}	$1.02^{+0.13}_{-0.11}$	$0.40^{+0.05}_{-0.05}$	$1.000^{+0.000}_{-0.984}$	$10.77^{+0.05}_{-0.05}$	$0.82^{+1.18}_{-0.53}$	67.2
		M05-krou	32^{+9}_{-6}	$3.00^{+0.38}_{-0.27}$	$0.80^{+0.05}_{-0.05}$	$0.020^{+0.000}_{-0.000}$	$11.11^{+0.04}_{-0.06}$	$0.89^{+1.18}_{-0.61}$	30.2
		P01-krou	$2.0^{+0.3}_{-0.2}$	$4.50^{+0.45}_{-0.48}$	$1.10^{+0.05}_{-0.07}$	$0.005^{+0.015}_{-0.000}$	$11.34^{+0.05}_{-0.05}$	$0.84^{+1.16}_{-0.58}$	40.9
		CB09-chab	$1.0^{+0.1}_{-0.1}$	$0.72^{+0.08}_{-0.07}$	$0.40^{+0.04}_{-0.05}$	$1.000^{+0.000}_{-0.000}$	$10.67^{+0.04}_{-0.05}$	$0.85^{+1.22}_{-0.57}$	34.8
		CB09-krou	63^{+8}_{-7}	$1.01^{+0.12}_{-0.10}$	$0.31^{+0.05}_{-0.04}$	$1.000^{+1.851}_{-0.000}$	$10.78^{+0.05}_{-0.04}$	$0.83^{+1.20}_{-0.53}$	32.8
		M05-krou	$1.0^{+0.1}_{-0.1}$	$4.00^{+0.50}_{-0.35}$	$0.70^{+0.06}_{-0.05}$	$0.020^{+0.000}_{-0.000}$	$11.17^{+0.05}_{-0.04}$	$0.64^{+0.91}_{-0.42}$	29.5
		M05-krou	31^{+5}_{-4}	$2.94^{+0.33}_{-0.34}$	$0.81^{+0.05}_{-0.06}$	$0.020^{+0.000}_{-0.000}$	$11.11^{+0.05}_{-0.03}$	$0.78^{+1.10}_{-0.52}$	29.2
		M05-krou	18^{+4}_{-4}	$2.98^{+0.62}_{-0.26}$	$0.80^{+0.07}_{-0.07}$	$0.020^{+0.000}_{-0.000}$	$11.11^{+0.06}_{-0.04}$	$0.67^{+0.97}_{-0.46}$	11.1
		P01-krou	$1.0^{+0.1}_{-0.1}$	$4.53^{+0.44}_{-0.51}$	$0.90^{+0.06}_{-0.04}$	$0.020^{+0.000}_{-0.015}$	$11.30^{+0.04}_{-0.04}$	$0.74^{+1.09}_{-0.51}$	37.2
		P01-krou	20^{+2}_{-2}	$4.44^{+0.48}_{-0.39}$	$1.10^{+0.03}_{-0.05}$	$0.005^{+0.000}_{-0.000}$	$11.34^{+0.05}_{-0.04}$	$0.77^{+0.98}_{-0.55}$	11.7
J123627.17+620756.57	1.3950	BC03-chab	398^{+54}_{-43}	$2.00^{+0.25}_{-0.21}$	$0.20^{+0.05}_{-0.05}$	$0.200^{+0.000}_{-0.000}$	$10.62^{+0.04}_{-0.06}$	$1.45^{+1.97}_{-1.04}$	56.1
		CB09-chab	63^{+8}_{-6}	$0.51^{+0.07}_{-0.05}$	$0.20^{+0.05}_{-0.05}$	$1.000^{+0.000}_{-0.000}$	$10.31^{+0.05}_{-0.05}$	$2.28^{+2.95}_{-1.70}$	52.5
		CB09-krou	501^{+65}_{-48}	$2.60^{+0.29}_{-0.29}$	$0.00^{+0.05}_{-0.00}$	$0.200^{+0.000}_{-0.180}$	$10.67^{+0.05}_{-0.05}$	$2.28^{+2.91}_{-1.65}$	71.7
		M05-krou	631^{+80}_{-64}	$3.00^{+0.34}_{-0.33}$	$0.20^{+0.05}_{-0.05}$	$0.020^{+0.000}_{-0.000}$	$10.62^{+0.05}_{-0.05}$	$1.68^{+2.16}_{-1.21}$	49.1
		P01-krou	251^{+37}_{-28}	$0.99^{+0.09}_{-0.08}$	$0.40^{+0.06}_{-0.05}$	$1.000^{+1.539}_{-0.603}$	$10.71^{+0.05}_{-0.04}$	$2.23^{+2.79}_{-1.63}$	36.3
		BC03-chab	199^{+20}_{-19}	$1.03^{+0.13}_{-0.13}$	$0.46^{+0.06}_{-0.14}$	$0.400^{+0.598}_{-0.206}$	$10.58^{+0.04}_{-0.04}$	$1.67^{+2.25}_{-1.19}$	39.1
		CB09-chab	101^{+10}_{-9}	$0.73^{+0.08}_{-0.07}$	$0.00^{+0.05}_{-0.00}$	$1.000^{+0.000}_{-0.615}$	$10.35^{+0.04}_{-0.05}$	$2.17^{+2.76}_{-1.64}$	28.6
		CB09-chab	22^{+3}_{-3}	$0.50^{+0.05}_{-0.06}$	$0.30^{+0.03}_{-0.04}$	$0.400^{+0.000}_{-0.396}$	$10.32^{+0.04}_{-0.03}$	$1.90^{+2.63}_{-1.42}$	15.0
		CB09-krou	181^{+29}_{-64}	$0.93^{+0.15}_{-0.18}$	$0.14^{+0.14}_{-0.09}$	$1.000^{+0.000}_{-0.802}$	$10.46^{+0.05}_{-0.05}$	$1.95^{+2.64}_{-1.38}$	19.8
		M05-krou	162^{+25}_{-23}	$1.50^{+0.20}_{-0.15}$	$0.00^{+0.05}_{-0.00}$	$0.020^{+3.084}_{-0.000}$	$10.41^{+0.06}_{-0.05}$	$2.16^{+2.85}_{-1.66}$	35.4
		M05-krou	997^{+133}_{-116}	$4.01^{+0.49}_{-0.40}$	$0.29^{+0.05}_{-0.04}$	$0.020^{+0.000}_{-0.000}$	$10.73^{+0.04}_{-0.05}$	$2.04^{+2.63}_{-1.64}$	15.5
		P01-krou	663^{+118}_{-74}	$2.51^{+0.23}_{-0.25}$	$0.22^{+0.40}_{-0.05}$	$0.200^{+0.199}_{-0.180}$	$10.75^{+0.05}_{-0.05}$	$2.05^{+2.69}_{-1.55}$	28.6
		P01-krou	496^{+50}_{-51}	$1.95^{+0.27}_{-0.24}$	$0.12^{+0.06}_{-0.06}$	$0.400^{+0.000}_{-0.200}$	$10.69^{+0.06}_{-0.04}$	$1.84^{+2.50}_{-1.35}$	24.7
		P01-krou	360^{+47}_{-59}	$1.46^{+0.19}_{-0.28}$	$0.32^{+0.21}_{-0.13}$	$0.400^{+0.602}_{-0.380}$	$10.69^{+0.05}_{-0.06}$	$1.60^{+2.12}_{-1.25}$	10.4
J123738.71+621727.86	1.2907	BC03-chab	57^{+9}_{-9}	$2.62^{+0.29}_{-0.29}$	$0.20^{+0.05}_{-0.04}$	$0.200^{+0.000}_{-0.000}$	$11.18^{+0.05}_{-0.04}$	$0.26^{+0.27}_{-0.24}$	91.1
		CB09-chab	63^{+7}_{-6}	$1.01^{+0.12}_{-0.10}$	$0.00^{+0.04}_{-0.00}$	$1.000^{+0.000}_{-0.000}$	$10.83^{+0.05}_{-0.05}$	$1.20^{+1.69}_{-0.82}$	100.0
		CB09-krou	70^{+13}_{-10}	$1.01^{+0.10}_{-0.12}$	$0.10^{+0.04}_{-0.05}$	$1.000^{+0.000}_{-0.000}$	$10.91^{+0.04}_{-0.04}$	$1.27^{+1.79}_{-0.86}$	41.6
		M05-krou	$1.0^{+0.1}_{-0.1}$	$3.98^{+0.42}_{-0.38}$	$0.51^{+0.04}_{-0.05}$	$0.020^{+0.000}_{-0.000}$	$11.31^{+0.04}_{-0.04}$	$0.46^{+0.48}_{-0.44}$	100.0
		P01-krou	500^{+55}_{-60}	$3.47^{+0.34}_{-0.32}$	$0.20^{+0.05}_{-0.04}$	$0.200^{+0.000}_{-0.000}$	$11.23^{+0.05}_{-0.05}$	$1.12^{+1.56}_{-0.74}$	72.6
		CB09-krou	135^{+20}_{-16}	$2.65^{+0.28}_{-0.29}$	$0.10^{+0.04}_{-0.04}$	$0.200^{+0.000}_{-0.000}$	$11.15^{+0.05}_{-0.05}$	$1.15^{+1.61}_{-0.79}$	36.6
		CB09-krou	$1.0^{+0.1}_{-0.1}$	$1.03^{+0.09}_{-0.13}$	$0.00^{+0.03}_{-0.00}$	$1.000^{+0.000}_{-0.000}$	$10.88^{+0.04}_{-0.04}$	$0.97^{+1.31}_{-0.69}$	16.0
		P01-krou	257^{+39}_{-30}	$2.55^{+0.43}_{-0.26}$	$0.29^{+0.06}_{-0.05}$	$0.200^{+0.000}_{-0.181}$	$11.21^{+0.05}_{-0.04}$	$1.24^{+1.75}_{-0.85}$	15.9
		P01-krou	$1.0^{+0.1}_{-0.1}$	$3.00^{+0.43}_{-0.23}$	$0.10^{+0.05}_{-0.05}$	$0.200^{+0.000}_{-0.000}$	$11.21^{+0.06}_{-0.05}$	$0.96^{+1.61}_{-0.68}$	11.5

Notes. Results of the SPS modeling of the SEDs of massive quiescent galaxies at $1.0 < z < 1.4$. Averages and $\pm 1\sigma$ values are quoted for each parameter. First five rows for each galaxy present the results for the most statistically significant solution for each one of the SPS libraries presented in the text. Next, secondary solutions are given (if available). (1) Name of the galaxy (including J2000 coordinates). (2) Spectroscopic redshift from the literature (see the text for references). (3) Stellar population models and IMF. (4) Exponential decay factor and uncertainty of the best-fitting model (in Myr). (5) Age and uncertainty (in Gyr) of the best-fitting model. (6) Extinction in the V-band and uncertainty (in mag) of the best-fitting model. (7) Metallicity and uncertainty (solar units) of the best-fitting model. (8) Stellar mass and uncertainty (solar units). (9) Median and 68% range for the goodness of the fit (χ^2 value). (10) Statistical significance of this solution (in %); only solutions with a significance above 10% are shown.

(This table is available in its entirety in a machine-readable form in theonline journal. A portion is shown here for guidance regarding its form and content.)

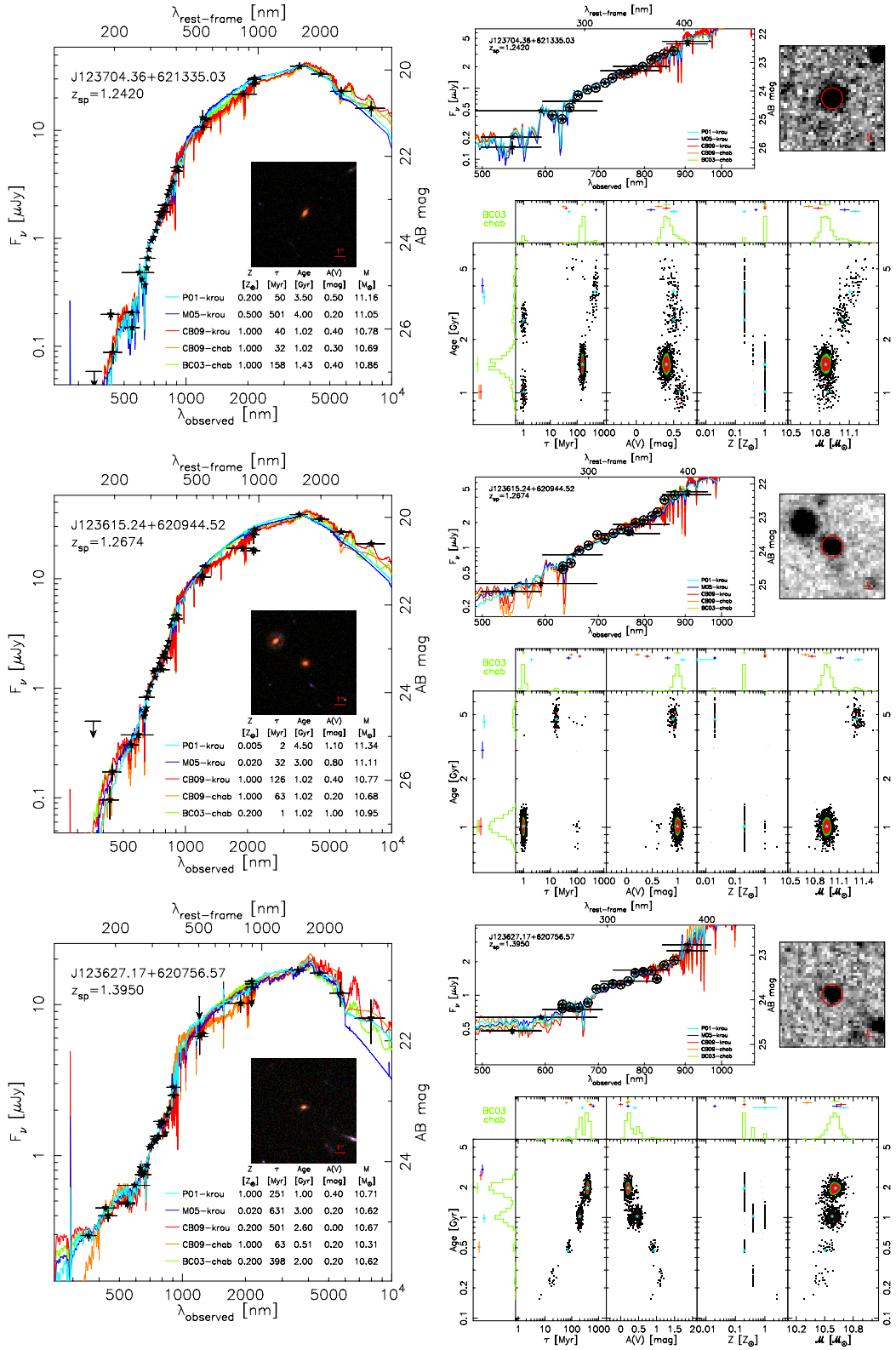

Figure 12. Three examples (one per row) of the SPS models carried out on quiescent massive galaxies with spectroscopic redshifts at $z > 1$. Each row shows the entire UV-to-MIR SED of a galaxy, along with the best fits for different modeling libraries (see the text for details), and an RGB $10'' \times 10''$ postage stamp image of the source built from *HST* data. The results for the best-fitting model are also given for each library, including ($Z/Z_\odot$, τ/Gyr, t/Gyr, $A(V)$/mag, $M/M_\odot$). Photometric data points include uncertainties and the width of the filter. To the right of the general SED, we show a close-up of the spectral region covered by SHARDS. In the top-right corner, we depict a postage stamp image of the galaxy in the F687W17 SHARDS band. Its size is $10'' \times 10''$, and the $1''$ radius red circle marks the galaxy. The bottom-right panel shows the position of the different model solutions derived with our Monte Carlo method to determine uncertainties and degeneracies. The data points correspond to our fiducial model: BC03-chab. We depict all the 1000 solutions in different planes: age–τ, age–extinction, age–metallicity, and age–mass. For the most statistically significant cluster, we mark the average solution with a star, the 1σ area is filled in red, and the 2σ region in green. For the rest of solutions with a significance above 10%, we mark the average with a star, and the area corresponding to 1σ with a red line. Histograms for the different parameters are also given, marking the average and 1σ values for the different models mentioned in the text (color code as in the left panel).

(A color version of this figure is available in the online journal.)

solution involving a shorter and younger burst ($\tau \sim 150$ Myr and age 1.8 Gyr), and a negligible fraction of solutions would favor even lower *e*-folding times and ages. When adding the SHARDS data to the fits, a solution with $\tau \sim 150$ Myr and $t \sim 1.5$ Gyr shows the largest statistical weight. This solution is consistent, within uncertainties, with one of the solutions found when fitting the broad-band data alone, although a slightly younger burst is favored in the SHARDS fluxes (age ∼1.5 Gyr instead of ∼2 Gyr).

In the case of J123615.24 + 620944.52 ($z = 1.2674$), the broad-band data provide a wide range of roughly equally significant solutions. Each one has 20–30% statistical significance. They show different values of extinction (differences of up to 0.5 mag from one solution to another), metallicity, and *e*-folding times (from an SSP to almost 200 Myr), while ages do not vary wildly (all solutions predict ages slightly above 1 Gyr). The SHARDS data break most of this degeneracy and mostly favor a 1 Gyr old SSP with $A(V) = 1$ mag. This is one of the largest extinctions in our sample, which could explain the relatively high flux at 8 μm, perhaps revealing the presence of polycyclic aromatic hydrocarbons (see Figure 12). Moreover, this galaxy has a very red companion located 3″ away to the NE (26 kpc), also at $z_{sp} = 1.2630$. This source is clearly detected at 24 μm, which might be hiding some residual MIPS emission for our galaxy, and provides an SFR $\sim 20\ M_{\odot}\ \mathrm{yr}^{-1}$. A possible interaction between the two objects could have switched on the star formation and then stopped recently, thus explaining the relatively high extinction.

In the case of J123627.17 + 620756.57 ($z = 1.3950$), both the broad-band data alone and the whole photometric information including SHARDS data favor at the approximately 60% significance level an SFH with an *e*-folding time around 400 Myr and ∼2 Gyr old, with $A(V) = 0.2$ mag. The SHARDS data help to discard some solutions found with only broad-band data which indicate very young and short bursts with high extinction (1 mag).

5.4. Examples of the SPS Results Including SHARDS Data

In Figure 12, we show the complete SEDs of the examples presented in the last subsection. We also present the best-fitting models for the different libraries considered in this paper, along with a close-up into the rest-frame UV/optical range probed by the SHARDS data. We include several plots showing the results of the synthesis models and the clustering analysis of the solutions. Finally, we also provide postage stamp images in the *HST* and SHARDS filters.

The galaxy shown at the top of Figure 12 lies at $z \sim 1.2420$ and our currently available SHARDS data cover the $\mathrm{Mg_{UV}}$ absorption feature. The SPS analysis for the BC03-chab fiducial models shows that there are at least four different clusters of solutions. The dominant cluster (76% statistical weight) is consistent with a short starburst ($\tau \sim 150$ Myr) with solar metallicity and relatively low extinction, $A(V) = 0.4$ mag. Among the other clusters, all of them showing statistical significances below 10%, we find a longer, lower abundance, and older burst ($\tau \sim 600$ Myr, $t \sim 4$ Gyr, $Z = Z_{\odot}/5$), and very short bursts (almost SSPs) with an age between 1 and 3 Gyr. These clusters share very similar extinction values [$A(V) = 0.4$ mag], with shorter bursts being more attenuated. Note that the latter are significantly less statistically representative than the former (i.e., the models favor a 150 Myr burst). We estimate a stellar mass within an interval around $10^{10.8}$–$10^{11.1}\ M_{\odot}$. Interestingly, although all different libraries obtain similarly good fits (i.e., similar reduced χ^2 values), they provide significantly different values for the relevant parameters, especially for the age and τ values. P01-krou and M05-krou favor the longest, oldest, less metallic, and higher mass solution, while BC03 and CB09 models for different IMFs are all consistent with shorter and younger bursts.

The second example in Figure 12 shows a $z = 1.2674$ galaxy where we have also been able to measure the $\mathrm{Mg_{UV}}$ absorption (but only the reddest part) with the SHARDS data available so far, apart from other spectral features such as the bluest part of the 4000 Å (or Balmer) break. The SPS degeneracies are considerably smaller than in the first example. Indeed, there is a dominant solution corresponding to a star-forming burst with $\tau \sim 1$ Myr (an SSP), age around 1 Gyr, $A(V) \sim 1.0$ mag, sub-solar metallicity, and mass around $10^{11.0}\ M_{\odot}$. Although this solution clearly dominates (90% probability) for the fiducial model, BC03-chab, other libraries again achieve different results, although with very similar statistical weight (i.e., one solution dominates for all different models). Note that the different libraries provide very similar results in the UV/optical part of the SED, but differ significantly in the *H* band and beyond the 1.6 μm bump, where BC03 and CB09 models reproduce the data more closely.

Finally, the last example in Figure 12 shows one of the sources at the highest redshifts in our sample of massive quiescent galaxies, $z \sim 1.4$. In this case, two solutions show similar significances, with *e*-folding times $\tau \sim$ 200–400 Myr, age around 1–2 Gyr, $A(V) = 0.2$–0.4 mag, sub-solar metallicity and mass $10^{10.6}\ M_{\odot}$. Similarly to the behavior of the different libraries in the previous example, in this case different models also obtain different estimations for the relevant parameters, especially age. *H*-band data probing the wavelength range around the rest-frame *RI* bands would most probably solve completely the degeneracy between the models.

5.5. Goodness of the Fits

It is interesting to discuss the properties of the sample and the goodness of the fits for the different SPS libraries. Concerning the latter, a very significant fraction of the whole sample, around 95% of all galaxies, is better fitted by the BC03-chab models, i.e., these models provide better reduced χ^2 values than any other code and IMF. This is the main reason for our choice of the BC03-chab models as fiducial in this paper. The rest of the best fits correspond to the CB09-krou and P01-krou models (∼2%–4% of sources each). After the best-fitting code, the second most preferred library and IMF is M05-krou, which gives the second best solution for 93% of the sources, with the rest of the second best solutions corresponding to P01-krou. Note that among the two models sharing the same library but with different IMFs, CB09-chab and CB09-krou, the Kroupa IMF provides the best results, but since the best-fitting code is BC03-chab, it seems that the goodness of the fit is more related to the SPS library than to the choice of IMF, i.e., based on the analysis of the goodness of the fits we cannot claim that one IMF works better than another.

To further test this result, indicating a preference for the BC03 models for the vast majority of sources, we repeated the SPS analysis but only using the broad-band data, i.e., without introducing the SHARDS fluxes. Interestingly, the best fits were then achieved by the BC03 models for 15% of the sample, while CB09 and M05 models obtained the best fits for 20%–30% of the galaxies, and P01 for just 8%. This clearly demonstrates that the UV/optical part (more precisely, the 200 nm $\lesssim \lambda_{\mathrm{r-f}} \lesssim$ 400 nm

Table 3
Statistical Properties of the Stellar Populations in $z \sim 1$ Massive Quiescent Galaxies

Model	M ($M_\odot$)			τ (Myr)			Age (Gyr)			$A(V)$ (mag)			Z ($Z_\odot$)		
	All	Light	Heavy	All	Light	Heavy	All	Light	Heavy	All	Light	Heavy	All	Light	Heavy
BC03-chab	$10.67^{10.96}_{10.53}$	$10.54^{10.63}_{10.49}$	$10.86^{11.11}_{10.74}$	119^{280}_{50}	123^{309}_{50}	103^{173}_{54}	$1.4^{2.0}_{1.0}$	$1.4^{1.9}_{1.0}$	$1.6^{2.3}_{1.0}$	$0.50^{0.94}_{0.23}$	$0.48^{0.93}_{0.24}$	$0.50^{0.92}_{0.22}$	$1.000^{2.500}_{0.200}$	$1.0000^{2.500}_{0.200}$	$1.000^{2.500}_{0.200}$
CB09-chab	$10.50^{10.82}_{10.35}$	$10.38^{10.49}_{10.32}$	$10.69^{10.89}_{10.66}$	63^{151}_{9}	62^{157}_{40}	65^{129}_{7}	$1.0^{2.2}_{1.0}$	$1.1^{1.4}_{0.5}$	$1.9^{3.2}_{1.0}$	$0.30^{0.50}_{0.10}$	$0.45^{0.50}_{0.10}$	$0.30^{0.51}_{0.09}$	$1.000^{1.000}_{0.400}$	$1.0000^{1.000}_{0.400}$	$1.000^{1.192}_{0.400}$
CB09-krou	$10.67^{10.91}_{10.47}$	$10.53^{10.62}_{10.43}$	$10.79^{10.98}_{10.74}$	110^{436}_{38}	88^{494}_{15}	122^{194}_{61}	$1.0^{2.6}_{1.0}$	$1.6^{2.6}_{1.0}$	$1.5^{1.9}_{1.0}$	$0.40^{0.70}_{0.01}$	$0.27^{0.59}_{0.00}$	$0.40^{0.72}_{0.10}$	$1.000^{2.500}_{0.400}$	$1.0000^{2.500}_{0.400}$	$1.000^{2.500}_{0.374}$
M05-krou	$10.77^{11.19}_{10.36}$	$10.51^{10.72}_{10.25}$	$11.11^{11.32}_{10.84}$	162^{632}_{36}	158^{380}_{36}	375^{663}_{42}	$3.0^{4.0}_{1.5}$	$2.0^{3.0}_{0.9}$	$3.6^{4.1}_{3.0}$	$0.40^{0.80}_{0.20}$	$0.28^{0.40}_{0.20}$	$0.51^{0.84}_{0.37}$	$0.500^{1.000}_{0.020}$	$0.7500^{1.000}_{0.500}$	$0.020^{1.000}_{0.020}$
P01-krou	$10.79^{11.18}_{10.65}$	$10.70^{10.75}_{10.57}$	$11.15^{11.33}_{10.88}$	191^{500}_{23}	185^{396}_{25}	193^{909}_{19}	$1.6^{3.5}_{1.2}$	$1.5^{1.8}_{1.2}$	$2.6^{3.8}_{1.4}$	$0.50^{0.81}_{0.35}$	$0.50^{0.69}_{0.36}$	$0.50^{1.09}_{0.28}$	$1.000^{2.500}_{0.200}$	$1.0000^{2.458}_{1.000}$	$0.400^{2.500}_{0.020}$

Notes. Median values and quartiles for the distribution of stellar parameters of the sample of 27 massive quiescent galaxies at $z = 1.0$–1.4 obtained by fitting different stellar population models to broad-band and SHARDS data. Statistics are given for all the sample and for the two half-samples obtained by breaking it by stellar mass (using the median value for the results obtained with each model).

interval) of the SED is better reproduced by the BC03 models, while the fits to the global broad-band photometry up to the IRAC bands are similarly reproduced (roughly) by all codes (except P01).

Concerning the statistical significance of the best solution, typical values for all models are always higher than 75%, although they could be as low as 40% in a few cases. Three quarters of the sample have a dominant solution above 50% for all models and IMFs. The actual individual values of the statistical significance of the different clusters of solutions are similar for the different codes, but for virtually all sources the most concentrated solution is given by the BC03-chab models (the typical probability for the best solution is 90%) and M05-krou (88%). For the fits to broad-band fluxes only, these figures are smaller by ∼20%. Figure 11 shows the comparison of SPS solutions obtained when using only broad-band data, and when adding the SHARDS medium-band photometry, for the sources plotted in Figure 12.

5.6. Statistical Properties of the Sample and Systematics

Statistics on the main properties of the stellar populations in our sample of massive quiescent galaxies are given in Table 3. This statistical information is presented for the distinct SPS codes, and discussed in this section.

According to our fiducial BC03-chab models, the median stellar mass of our sample of 27 massive quiescent galaxies at $z > 1$ is $10^{10.7}\,M_\odot$. Typically, their stellar population is 1.5 Gyr old and was formed in a burst with solar or slightly sub-solar metallicity with an SFH characterized by an e-folding time $\tau \sim 150$ Myr, and currently presents a moderate extinction $A(V) \sim 0.5$ mag.

If we consider the average of the different stellar mass estimates obtained with the distinct codes and IMFs for a given galaxy, its typical rms is 0.15 dex, and for some galaxies can be as high as 0.27 dex. Most of this rms is due to systematic differences between the results obtained with different models and IMFs. According to our fiducial models, BC03-chab, masses for individual sources run from $10^{10.3}\,M_\odot$ to $10^{11.2}\,M_\odot$. BC03-chab provide, on average, larger masses than CB09-krou by ∼20% when comparing values for each galaxy, with differences as large as a factor of 2 (in both directions). CB09-chab models give masses smaller than BC03-chab by 30% on average, and up to a factor of 3. We note that differences between the two CB09 models with different IMFs are not just a constant offset, but are variable from galaxy to galaxy and dependent on other parameters such as age. M05-krou and P01-krou provide heavier masses than BC03-chab by 15% and 40% on average, respectively, with differences as high as a factor of 3–4. Note that the effects of the TP-AGB phase, which could in principle be studied by comparing classical models with libraries such as M05 or CB09, are complex, sometimes producing larger and sometimes smaller masses.

Extinctions show better agreement between different models. The average value for the sample is $A(V) = 0.5$ mag for our fiducial models, with a typical uncertainty of 0.2 mag. This is also the typical average systematic offset from one model to another. All models provide systematically lower extinctions than the BC03-chab models.

Our sample presents ages in the range 0.5–3.5 Gyr for our fiducial model BC03-chab. On average, BC03 and CB09 models provide similar ages within 10%, but differences from model to model among these libraries range from 0.2 to 3 Gyr for individual galaxies. M05-krou and P01-krou models provide, on average, older ages by 90% and 30%, respectively. These ages and systematic differences are in good agreement with the results found in the literature for $z \sim 1$ galaxies (see, e.g., Hathi et al. 2009; Whitaker et al. 2010, 2012).

The typical star formation timescale for our sample is $\tau \sim 150$ Myr for our fiducial models. For CB09 models and the two IMFs considered, τ values are, on average, 25% shorter. M05 and P01 results indicate longer e-folding timescales by 70% and 20%, respectively.

Concerning metallicities, for the BC03 models the average value is solar, and that is also the case for all the other codes, except M05 models, which provide an average value of 0.4 $Z_\odot$. Note that a photometric study such as ours has severe difficulties in determining accurate stellar metallicities and breaking degeneracies involving age, extinction, and metallicity (O'Connell 1986; Worthey 1994; Wuyts et al. 2009), but it is significant that all models provide consistent values near or slightly below the solar value (consistent with other works such as Hathi et al. 2009 or Ferreras et al. 2009; see also Dorman et al. 2003 and Kaviraj et al. 2007).

In summary, there is a significant scatter in the predicted parameters for our sample of massive galaxies by different SPS codes and IMFs. It seems that this scatter is preferentially linked to the stellar population codes, rather than to the IMF. BC03 (and Chabrier IMF) provide in virtually all cases the best solutions in terms of goodness of fit and statistical significance of the best solution, although the χ^2 differences between models are not statistically significant for individual galaxies. This preference is directly linked to the SHARDS data (probing the rest-frame UV/optical range), given that it is no longer seen when fitting broad-band fluxes only. The stellar population in our sample of massive galaxies at $z \sim 1$ is typically (according to our fiducial models, BC03-chab) 1.5 Gyr old, with a formation timescale

around 100–200 Myr, solar or slightly sub-solar metallicity, and moderate extinction $A(V) \sim 0.5$ mag.

5.7. Global Picture of the Formation of Massive Galaxies at $z \sim 1$

Our sample of massive quiescent galaxies at $z > 1$ is small and driven by the availability of spectroscopic redshifts. Consequently, its representativeness of the global population of such type of galaxies is highly uncertain. However, it is large enough to study whether there are significant differences in the stellar populations of galaxies as a function of mass. This is the base for the downsizing scenario of galaxy formation. To analyze this topic, we have divided our sample into two mass bins with the same number of galaxies. Note that the median mass of our sample is $10^{10.7}\,M_{\odot}$ for the BC03-chab models, slightly smaller than the $M^{*} \sim 10^{10.9}\,M_{\odot}$ value at $z = 1.0$–1.5[23] (Pérez-González et al. 2008; Marchesini et al. 2009), so our (limited and not statistically representative) sample does probe the masses around the knee of the mass function at redshift unity.

Figure 13 shows the SFHs of all galaxies in our sample for the SPS results obtained with the two best-fitting models, BC03 and M05. We have used a rainbow color code based on stellar mass: massive galaxies are plotted in yellow and redder colors, while lighter galaxies are depicted in green or bluer colors. According to the BC03 models, there is not a large difference in age and SFH between galaxies of different mass. However, there is a trend for the oldest galaxies to be among the most massive. In the case of the M05, a segregation in mass is more evident: the lightest galaxies preferentially show young stellar populations, while most of the heaviest galaxies were formed 3 Gyr before the epoch of observation ($z > 2$). In addition, some of the most massive galaxies show SFHs close to an SSP, also according to the M05 results.

The ages for the lightest half-sample range from 0.6 to 2.5 Gyr for BC03 models, and 0.2 to 3.5 Gyr for M05. For the most massive half of the sample, ages range from 1.0 to 2.7 Gyr according to BC03, and 2.9 to 5.0 Gyr for M05 results. On average, the most massive half of our sample harbors stellar populations that are 1.6 Gyr old, while the lightest-half are 20% younger for the results obtained with BC03 models. For M05 models, the difference is significantly larger: the heaviest galaxies show, on average, 4 Gyr old stellar populations, compared to 2 Gyr old stars for the lightest systems. Other libraries provide intermediate-results, i.e., a segregation in age of galaxies of different masses with larger differences than those for the BC03 models, but smaller than for the M05 code. If we only use broad-band data in our fits, the results are roughly unchanged for the M05, CB09, and P01 libraries, but the segregation is more significant for the BC03 code: it provides an average age of 2.5 Gyr for the most massive galaxies, and 1.5 Gyr for the lightest.

For our fiducial models, most galaxies present e-folding times around 100–300 Myr and peak SFRs around 400–500 $M_{\odot}\ \mathrm{yr}^{-1}$, but there are some examples which are characterized by shorter bursts and could reach even higher SFRs. For M05, e-folding times are larger (100–600 Myr) and peak SFRs are smaller. These SFR figures and duty cycles are typical of ULIRGs and/or submillimeter galaxies at $z \sim 2$ (e.g., Blain et al. 1999; Smail et al. 2002; Chapman et al. 2005; Pérez-González et al. 2005; Dey et al. 2008; Pope et al. 2008). They are also consistent with the SFRs predicted by cosmological simulations involving gas-rich mergers (e.g., Davé et al. 2010; Narayanan et al. 2010a, 2010b).

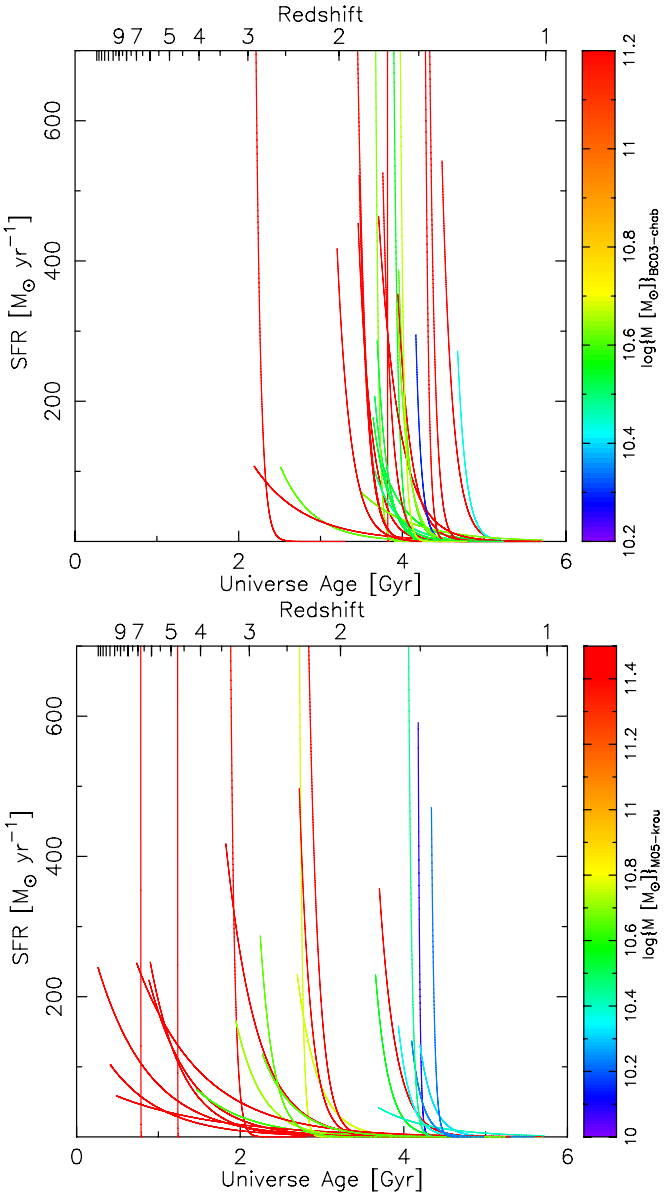

Figure 13. Star formation histories for 27 spectroscopically confirmed quiescent massive galaxies in GOODS-N. The rainbow-based color code differentiates galaxies according to stellar mass, with the most massive sources plotted in yellow or redder colors, and less massive galaxies plotted in green or bluer colors. The left panel shows the results for the BC03-chab stellar population synthesis models, and the right plot shows the results for M05-krou.

(A color version of this figure is available in the online journal.)

Our results are roughly consistent with those described in Ferreras et al. (2009) and Kaviraj et al. (2012). In Ferreras et al. (2009), they used CB09 models to fit optical low-resolution spectroscopic data of intermediate-redshift massive early-type galaxies. Based on these models, they found typical ages of 2–3 Gyr for their last redshift bin ($z > 0.9$), slightly dependent on stellar mass. No major differences were found in this paper in the star formation timescale as a function of mass. This agrees well with our ages around 1–2 Gyr for $z \sim 1.2$ (there is 1.2 Gyr difference in look-back time between $z = 0.9$ and

[23] Value obtained after accounting for differences in IMF and stellar population library between different works.

$z = 1.2$), and the very similar e-folding times for galaxies with different masses. Kaviraj et al. (2012), using CB09 models fitting broad-band data, found similar ages for massive galaxies up to $M \sim 10^{10.5}\,M_{\odot}$, and a trend at higher masses where heavier galaxies are older. However, we stress that our study points out that the mass–age relationship should be regarded with caution, given that it is highly dependent on the SPS code used in the SED fitting.

6. SUMMARY AND CONCLUSIONS

We have presented the basic characteristics of the survey for SHARDS, an ESO/GTC Large Program awarded 180 hr of observing time with the OSIRIS instrument on the 10.4 m GTC. The SHARDS project was devised to be able to measure absorption indices such as the Mg_{UV} or $D(4000)$ for galaxies at $z = 0.0$–2.5 through imaging data, and detect ELGs up to $z \sim 6$. For those purposes, SHARDS is obtaining imaging data in the GOODS-N field through 24 medium-band filters covering the wavelength range between 500 and 950 nm and reaching magnitude 26.5 in all bands. In addition, virtually all the images were obtained under sub-arcsec seeing conditions.

In this paper, we have presented the special reduction and calibration procedures used to analyze the SHARDS observations. The flux calibration has been carried out by comparison with *HST* and ground-based (Keck, CAHA 3.5 m telescope) spectra. The zero points have also been tested by comparing with synthetic magnitudes obtained from stellar population synthesis models fitting broad-band data. Overall, our procedure achieves an absolute photometric calibration uncertainty lower than 8% (typically 5%–7%).

In this paper, we have carried out a science verification of the main goals of SHARDS. We have shown how the SHARDS data are able to detect emission lines for low-, intermediate- and high-redshift sources. We have demonstrated that the depth and image quality of our survey allow us to select virtually all ELGs which have been already confirmed by the deepest spectroscopic surveys carried out in the GOODS-N field, such as TKRS and DEEP3. We have shown that we are able to extend these spectroscopic studies of ELGs to faint magnitudes (fainter than the typical spectroscopic limit, $RI \sim 24$–25 mag) and detect, for example, LAEs at $z \sim 5$. By combining all the SHARDS data and fitting stellar population synthesis models, we have also shown that we can measure EWs and fluxes for those emission lines. A comprehensive study of the population of ELGs detected by SHARDS in GOODS-N will be presented in a future paper (A. Cava et al. 2012, in preparation).

We have assessed the ability of the SHARDS data to detect, measure, and model absorption features in intermediate and high-z galaxies. For that purpose, we have analyzed the SHARDS data for all passively evolving galaxies at $z > 1$ counting with a spectroscopic redshift, whose SED should be dominated by absorption features. We have constructed a sample of 27 quiescent massive galaxies with spectroscopic redshifts at $1.01 < z < 1.43$ extracted from several sources and covered by the SHARDS data (and detected in all SHARDS bands, although this was not a requirement of the sample selection). For this sample, we have analyzed the entire SED from the UV to the MIR, including broad-band data from ground-based telescopes, *HST*, and *Spitzer*, as well as the SHARDS photometry. This analysis consists in fitting the SEDs with stellar population synthesis models assuming an exponentially decreasing SFH (τ models) and an extinction law described by Calzetti's law. We have not imposed any a priori limitations on the metallicity, τ value, or age. In order to study the robustness of the derived parameters, we have used a variety of stellar population libraries, namely: BC03, M05, CB09, and P01. Our fitting method includes a procedure to probe the typical degeneracies in this kind of study, such as those linked to age–metallicity or age–extinction. This procedure is based on a Monte Carlo method which assigns statistical significances to the different possible solutions found by the synthesis models.

Our results demonstrate that including the SHARDS spectrophotometric data in the analysis of the stellar populations in high-z passively evolving galaxies helps to break these degeneracies, although we do not fully succeed in this task. When using the SHARDS data, the statistical significance of the best solution (that with the highest significance) is typically 10%–20% larger than when fitting broad-band data alone. The typical value of the statistical significance of the best solution when fitting all available photometry is 75% (i.e., one solution is favored at the 75% probability level). Interestingly, among the different SPS libraries used in this paper, BC03 models (with a Chabrier IMF) provide the best fits (the ones with the best reduced χ^2 values) for more than 90% of the sample when fitting SHARDS and broad-band data. When only fitting broad-band data, all models are (roughly) equally good in reproducing the data. We conclude that BC03 models are the most suited to study the rest-frame UV/optical part (up to ∼400 nm) of the SEDs for our sample.

Taking into account all different models, we find that the stellar populations in our sample of passively evolving massive sources at $z > 1$ are typically 1.5–2.0 Gyr old, presenting typical τ values around 100–200 Myr, solar or slightly sub-solar metallicity, and V-band extinctions around 0.5 mag. However, significant systematic differences from one model library to another are found for individual sources, especially in the age and τ values. Stellar masses are better behaved, with the largest differences from one model to another being below 0.3 dex. Using an average of all the models, the typical masses of the galaxies in our sample are in the interval $10^{10.5}$–$10^{11.5}\,M_{\odot}$.

Dividing our sample of massive quiescent galaxies at $z > 1$ in half according to their stellar masses, we find that the most massive galaxies tend to be older for all libraries. The differences are small for BC03 results, and considerably larger for fits using M05, CB09, or P01 models. Just using broad-band data also produces a clearer age segregation in mass. Typically, for the M05 models, the lightest galaxies show ages around 2 Gyr, while the heaviest systems are 3–4 Gyr old on average, with some galaxies reaching ages around 5 Gyr (i.e., they started forming less than 1 Gyr after the big bang). No significant difference in the SFH is found between the most massive and lighter samples.

We acknowledge support from the Spanish Programa Nacional de Astronomía y Astrofísica under grants AYA2009-07723-E and AYA2009-10368. SHARDS has been funded by the Spanish MICINN/MINECO under the Consolider-Ingenio 2010 Program grant CSD2006-00070: First Science with the GTC. O.G.-M., C.M.-T., J.M.R.-E., and J.R.-Z. wish to acknowledge support from grant AYA2010-21887-C04-04. A.A.-H. and A.H.-C. acknowledge financial support from the Universidad de Cantabria through the Augusto G. Linares Program. This work has made use of the Rainbow Cosmological Surveys Database, which is operated by the Universidad Complutense de Madrid (UCM). This research has made use of the VizieR catalogue access tool, CDS, Strasbourg, France. Based on observations made with the Gran Telescopio Canarias (GTC),

installed at the Spanish Observatorio del Roque de los Muchachos of the Instituto de Astrofísica de Canarias, in the island of La Palma. We thank all the GTC Staff for their support and enthusiasm with the SHARDS project, and we especially acknowledge the help from Antonio Cabrera and René Rutten. The work is also based on observations collected at the Centro Astronómico Hispano Alemán (CAHA) at Calar Alto, operated jointly by the Max-Planck-Institut für Astronomie and the Instituto de Astrofísica de Andalucía (CSIC). We thank the referee for her/his very useful and positive comments.

REFERENCES

Abramo, L. R., Strauss, M. A., Lima, M., et al. 2012, MNRAS, 423, 3251
Arnouts, S., Walcher, C. J., Le Fvre, O., et al. 2007, A&A, 476, 137
Balogh, M. L., Morris, S. L., Yee, H. K. C., Carlberg, R. G., & Ellingson, E. 1999, ApJ, 527, 54
Barger, A. J., Cowie, L. L., & Wang, W.-H. 2008, ApJ, 689, 687
Barro, G., Pérez-González, P. G., Gallego, J., et al. 2011a, ApJS, 193, 13
Barro, G., Pérez-González, P. G., Gallego, J., et al. 2011b, ApJS, 193, 30
Bauer, A. E., Drory, N., Hill, G. J., & Feulner, G. 2005, ApJL, 621, 89
Baugh, C. M., Cole, S., Frenk, C. S., & Lacey, C. G. 1998, ApJ, 498, 504
Bell, E. F., Phleps, S., Somerville, R. S., et al. 2006, ApJ, 652, 270
Bell, E. F., Wolf, C., Meisenheimer, K., et al. 2004, ApJ, 608, 752
Benítez, N., Gaztañaga, E., Miquel, R., et al. 2009a, ApJ, 691, 241
Benítez, N., Moles, M., Aguerri, J. A. L., et al. 2009b, ApJL, 692, 5
Bertin, E. 2006, in ASP Conf. Ser. 351, Astronomical Data Analysis Software and Systems XV, ed. C. Gabriel, C. Arviset, D. Ponz, & S. Enrique (San Francisco, CA: ASP), 112
Bertin, E., & Arnouts, S. 1996, A&AS, 117, 393
Blain, A. W., Smail, I., Ivison, R. J., & Kneib, J.-P. 1999, MNRAS, 302, 632
Borch, A., Meisenheimer, K., Bell, E. F., et al. 2006, A&A, 453, 869
Bouwens, R. J., Illingworth, G. D., Blakeslee, J. P., & Franx, M. 2006, ApJ, 653, 53
Brammer, G. B., Whitaker, K. E., van Dokkum, P. G., et al. 2009, ApJL, 706, 173
Brammer, G. B., Whitaker, K. E., van Dokkum, P. G., et al. 2011, ApJ, 739, 24
Bruzual, A., & Charlot, S. 1993, ApJ, 405, 538
Bruzual, G. 1983, ApJ, 273, 105
Bruzual, G., & Charlot, S. 2003, MNRAS, 344, 1000
Burstein, D., Faber, S. M., Gaskell, C. M., & Krumm, N. 1984, ApJ, 287, 586
Calzetti, D., Armus, L., Bohlin, R. C., et al. 2000, ApJ, 533, 682
Caputi, K. I., Dole, H., Lagache, G., et al. 2006, ApJ, 637, 727
Cardamone, C. N., van Dokkum, P. G., Urry, C. M., et al. 2010, ApJS, 189, 270
Cardelli, J. A., Clayton, G. C., & Mathis, J. S. 1989, ApJ, 345, 245
Cepa, J. 2010, in Highlights of Spanish Astrophysics V, ed. J. M. Diego, L. J. Goicoechea, J. I. González-Serrano, & J. Gorgas (Berlin: Springer), 15
Cepa, J., Bongiovanni, A., Pérez-García, A. M., et al. 2011, in Highlights of Spanish Astrophysics VI, ed. M. R. Zapatero Osorio, J. Gorgas, J. Maíz Apellániz, J. R. Pardo, & A. Gil de Paz, 167
Chabrier, G. 2003, ApJL, 586, 133
Chapman, S. C., Blain, A. W., Smail, I., & Ivison, R. J. 2005, ApJ, 622, 772
Charlot, S., & Longhetti, M. 2001, MNRAS, 323, 887
Cimatti, A., Cassata, P., Pozzetti, L., et al. 2008, A&A, 482, 21
Cimatti, A., Daddi, E., Renzini, A., et al. 2004, Natur, 430, 184
Cole, S., Lacey, C. G., Baugh, C. M., & Frenk, C. S. 2000, MNRAS, 319, 168
Colless, M., Dalton, G., Maddox, S., et al. 2001, MNRAS, 328, 1039
Conselice, C. J., Bershady, M. A., Dickinson, M., & Papovich, C. 2003, AJ, 126, 1183
Conselice, C. J., Bundy, K., Trujillo, I., et al. 2007, MNRAS, 381, 962
Cooper, M. C., Aird, J. A., Coil, A. L., et al. 2011, ApJS, 193, 14
Cowie, L. L., Barger, A. J., Hu, E. M., Capak, P., & Songaila, A. 2004, AJ, 127, 3137
Cowie, L. L., Songaila, A., Hu, E. M., & Cohen, J. G. 1996, AJ, 112, 839
Croton, D. J., Springel, V., White, S. D. M., et al. 2006, MNRAS, 365, 11
Daddi, E., Cimatti, A., Renzini, A., et al. 2004, ApJ, 617, 746
Daddi, E., Dickinson, M., Chary, R., et al. 2005a, ApJL, 631, 13
Daddi, E., Renzini, A., Pirzkal, N., et al. 2005b, ApJ, 626, 680
Davé, R., Finlator, K., Oppenheimer, B. D., et al. 2010, MNRAS, 404, 1355
Dekel, A., Birnboim, Y., Engel, G., et al. 2009, Natur, 457, 451
De Lucia, G., & Blaizot, J. 2007, MNRAS, 375, 2
Dey, A., Soifer, B. T., Desai, V., et al. 2008, ApJ, 677, 943
Dorman, B., O'Connell, R. W., & Rood, R. T. 2003, ApJ, 591, 878
Eggen, O. J., Lynden-Bell, D., & Sandage, A. R. 1962, ApJ, 136, 748
Eisenstein, D. J., Zehavi, I., Hogg, D. W., et al. 2005, ApJ, 633, 560
Elbaz, D., Dickinson, M., Hwang, H. S., et al. 2011, A&A, 533, A119
Ellis, R. S., Abraham, R. G., Brinchmann, J., & Menanteau, F. 2000, A&G, 41, 020000
Ellis, R., Santos, M. R., Kneib, J.-P., & Kuijken, K. 2001, ApJL, 560, 119
Elsner, F., Feulner, G., & Hopp, U. 2008, A&A, 477, 503
Elston, R., Rieke, G. H., & Rieke, M. J. 1988, ApJL, 331, 77
Faber, S. M., Tremaine, S., Ajhar, E. A., et al. 1997, AJ, 114, 1771
Faber, S. M., Willmer, C. N. A., Wolf, C., et al. 2007, ApJ, 665, 265
Ferreras, I., Pasquali, A., Khochfar, S., et al. 2012, AJ, 144, 47
Ferreras, I., Pasquali, A., Malhotra, S., et al. 2009, ApJ, 706, 158
Ferreras, I., & Yi, S. K. 2004, MNRAS, 350, 1322
Fioc, M., & Rocca-Volmerange, B. 1997, A&A, 326, 950
Fontana, A., Salimbeni, S., Grazian, A., et al. 2006, A&A, 459, 745
Förster Schreiber, N. M., van Dokkum, P. G., Franx, M., et al. 2004, ApJ, 616, 40
Franx, M., Labbé, I., Rudnick, G., et al. 2003, ApJL, 587, 79
Frayer, D. T., Huynh, M. T., Chary, R., et al. 2006, ApJL, 647, 9
Gallazzi, A., Charlot, S., Brinchmann, J., White, S. D. M., & Tremonti, C. A. 2005, MNRAS, 362, 41
Gaztañaga, E., Cabré, A., & Hui, L. 2009, MNRAS, 399, 1663
Giavalisco, M., Ferguson, H. C., Koekemoer, A. M., et al. 2004, ApJL, 600, 93
Gilbank, D. G., Baldry, I. K., Balogh, M. L., Glazebrook, K., & Bower, R. G. 2010, MNRAS, 405, 2594
Glazebrook, K., Abraham, R. G., McCarthy, P. J., et al. 2004, Natur, 430, 181
Grogin, N. A., Kocevski, D. D., Faber, S. M., et al. 2011, ApJS, 197, 35
Guaita, L., Gawiser, E., Padilla, N., et al. 2010, ApJ, 714, 255
Guo, Q., White, S., Li, C., & Boylan-Kolchin, M. 2010, MNRAS, 404, 1111
Hathi, N. P., Ferreras, I., Pasquali, A., et al. 2009, ApJ, 690, 1866
Hayes, M., Östlin, G., Schaerer, D., et al. 2010a, Natur, 464, 562
Hayes, M., Schaerer, D., & Östlin, G. 2010b, A&A, 509, L5
Heavens, A., Panter, B., Jimenez, R., & Dunlop, J. 2004, Natur, 428, 625
Henriques, B. M. B., White, S. D. M., Lemson, G., et al. 2012, MNRAS, 421, 2904
Ilbert, O., Capak, P., Salvato, M., et al. 2009, ApJ, 690, 1236
Ilbert, O., Salvato, M., Le Floc'h, E., et al. 2010, ApJ, 709, 644
Kashikawa, N., Shimasaku, K., Malkan, M. A., et al. 2006, ApJ, 648, 7
Kauffmann, G., Colberg, J. M., Diaferio, A., & White, S. D. M. 1999, MNRAS, 303, 188
Kauffmann, G., Heckman, T. M., White, S. D. M., et al. 2003a, MNRAS, 341, 33
Kauffmann, G., Heckman, T. M., White, S. D. M., et al. 2003b, MNRAS, 341, 54
Kauffmann, G., White, S. D. M., & Guiderdoni, B. 1993, MNRAS, 264, 201
Kaviraj, S., Rey, S.-C., Rich, R. M., Yoon, S.-J., & Yi, S. K. 2007, MNRAS, 381, L74
Kaviraj, S., Cohen, S., Ellis, R. S., et al. 2012, MNRAS, in press (arXiv:1206.2360)
Kewley, L. J., & Dopita, M. A. 2002, ApJS, 142, 35
Klypin, A., Kravtsov, A. V., Valenzuela, O., & Prada, F. 1999, ApJ, 522, 82
Kodaira, K., Taniguchi, Y., Kashikawa, N., et al. 2003, PASJ, 55, L17
Koekemoer, A. M., Faber, S. M., Ferguson, H. C., et al. 2011, ApJS, 197, 36
Komatsu, E., Smith, K. M., Dunkley, J., et al. 2011, ApJS, 192, 18
Kravtsov, A. V., Gnedin, O. Y., & Klypin, A. A. 2004, ApJ, 609, 482
Kriek, M., Labbé, I., Conroy, C., et al. 2010, ApJL, 722, 64
Kriek, M., van Dokkum, P. G., Franx, M., et al. 2006, ApJL, 649, 71
Kriek, M., van Dokkum, P. G., Franx, M., et al. 2008, ApJ, 677, 219
Kriek, M., van Dokkum, P. G., Whitaker, K. E., et al. 2011, ApJ, 743, 168
Kron, R. G. 1980, ApJS, 43, 305
Kroupa, P. 2001, MNRAS, 322, 231
Kümmel, M., Walsh, J. R., Pirzkal, N., Kuntschner, H., & Pasquali, A. 2009, PASP, 121, 59
Lacey, C., & Cole, S. 1993, MNRAS, 262, 627
Lara-López, M. A., Cepa, J., Castaeda, H., et al. 2011, PASP, 123, 252
Larson, R. B. 1974, MNRAS, 166, 585
Leauthaud, A., Tinker, J., Bundy, K., et al. 2012, ApJ, 744, 159
Lee, J. C., Ly, C., Spitler, L., et al. 2012, PASP, 124, 782
Le Fèvre, O., Abraham, R., Lilly, S. J., et al. 2000, MNRAS, 311, 565
Li, C., & White, S. D. M. 2009, MNRAS, 398, 2177
López-Sanjuan, C., Balcells, M., Pérez-González, P. G., et al. 2009, A&A, 501, 505
Lotz, J. M., Davis, M., Faber, S. M., et al. 2008, ApJ, 672, 177
Lotz, J. M., Ferguson, H. C., & Bohlin, R. C. 2000, ApJ, 532, 830
Lutz, D., Poglitsch, A., Altieri, B., et al. 2011, A&A, 532, A90
Ly, C., Lee, J. C., Dale, D. A., et al. 2011, ApJ, 726, 109
Ly, C., Malkan, M. A., Kashikawa, N., et al. 2007, ApJ, 657, 738
Maraston, C. 2005, MNRAS, 362, 799

Marchesini, D., van Dokkum, P. G., Förster Schreiber, N. M., et al. 2009, ApJ, 701, 1765
Mayya, Y. D., Rosa González, D., Vega, O., et al. 2012, PASP, 124, 895
McCarthy, P. J., Le Borgne, D., Crampton, D., et al. 2004, ApJL, 614, 9
Méndez-Abreu, J., Sánchez Almeida, J., Muñoz-Tun, C., et al. 2011, PASP, 123, 1107
Miley, G. K., Overzier, R. A., Zirm, A. W., et al. 2006, ApJL, 650, 29
Moles, M., Bentez, N., Aguerri, J. A. L., et al. 2008, AJ, 136, 1325
Muzzin, A., Wilson, G., Yee, H. K. C., et al. 2012, ApJ, 746, 188
Narayanan, D., Dey, A., Hayward, C. C., et al. 2010a, MNRAS, 407, 1701
Narayanan, D., Hayward, C. C., Cox, T. J., et al. 2010b, MNRAS, 401, 1613
Newman, A. B., Ellis, R. S., Treu, T., & Bundy, K. 2010, ApJL, 717, 103
Nicol, M.-H., Meisenheimer, K., Wolf, C., & Tapken, C. 2011, ApJ, 727, 51
Nilsson, K. K., Tapken, C., Møller, P., et al. 2009, A&A, 498, 13
O'Connell, R. W. 1986, in Stellar Populations, ed. C. A. Norman, A. Renzini, & M. Tosi, 167
Oliver, S. J., Wang, L., Smith, A. J., et al. 2010, A&A, 518, L21
Ouchi, M., Shimasaku, K., Akiyama, M., et al. 2008, ApJS, 176, 301
Ouchi, M., Shimasaku, K., Furusawa, H., et al. 2003, ApJ, 582, 60
Ouchi, M., Shimasaku, K., Okamura, S., et al. 2004, ApJ, 611, 660
Pacifici, C., Charlot, S., Blaizot, J., & Brinchmann, J. 2012, MNRAS, 421, 2002
Papovich, C., Dickinson, M., & Ferguson, H. C. 2001, ApJ, 559, 620
Papovich, C., Moustakas, L. A., Dickinson, M., et al. 2006, ApJ, 640, 92
Pascual, S., Gallego, J., Aragón-Salamanca, A., & Zamorano, J. 2001, A&A, 379, 798
Percival, W. J., Baugh, C. M., Bland-Hawthorn, J., et al. 2001, MNRAS, 327, 1297
Percival, W. J., Reid, B. A., Eisenstein, D. J., et al. 2010, MNRAS, 401, 2148
Pérez-González, P. G., Gil de Paz, A., Zamorano, J., et al. 2003, MNRAS, 338, 525
Pérez-González, P. G., Rieke, G. H., Egami, E., et al. 2005, ApJ, 630, 82
Pérez-González, P. G., Rieke, G. H., Villar, V., et al. 2008, ApJ, 675, 234
Pforr, J., Maraston, C., & Tonini, C. 2012, MNRAS, 422, 3285
Pirzkal, N., Burgasser, A. J., Malhotra, S., et al. 2009, ApJ, 695, 1591
Pirzkal, N., Xu, C., Malhotra, S., et al. 2004, ApJS, 154, 501
Pope, A., Bussmann, R. S., Dey, A., et al. 2008, ApJ, 689, 127
Quilis, V., & Trujillo, I. 2012, ApJL, 752, 19
Reddy, N. A., Erb, D. K., Steidel, C. C., et al. 2005, ApJ, 633, 748
Reddy, N. A., Steidel, C. C., Erb, D. K., Shapley, A. E., & Pettini, M. 2006, ApJ, 653, 1004
Renzini, A. 2006, ARA&A, 44, 141
Ricciardelli, E., & Franceschini, A. 2010, A&A, 518, A14
Rix, H.-W., Barden, M., Beckwith, S. V. W., et al. 2004, ApJS, 152, 163
Rodriguez-Espinosa, J. M., Gonzalez-Martin, O., Lopez-Aguerri, J. A., et al. 2012, arXiv:1201.4727
Saracco, P., Longhetti, M., Severgnini, P., et al. 2005, MNRAS, 357, L40
Scoville, N., Aussel, H., Benson, A., et al. 2007, ApJS, 172, 150
Searle, L., & Zinn, R. 1978, ApJ, 225, 357
Shioya, Y., Taniguchi, Y., Sasaki, S. S., et al. 2008, ApJS, 175, 128
Smail, I., Ivison, R. J., Blain, A. W., & Kneib, J.-P. 2002, MNRAS, 331, 495
Sobral, D., Best, P. N., Geach, J. E., et al. 2009, MNRAS, 398, 75
Sobral, D., Best, P. N., Matsuda, Y., et al. 2012, MNRAS, 420, 1926
Somerville, R. S., Hopkins, P. F., Cox, T. J., Robertson, B. E., & Hernquist, L. 2008, MNRAS, 391, 481
Somerville, R. S., & Primack, J. R. 1999, MNRAS, 310, 1087
Spergel, D. N., Bean, R., Doré, O., et al. 2007, ApJS, 170, 377
Spinrad, H., Dey, A., Stern, D., et al. 1997, ApJ, 484, 581
Springel, V., White, S. D. M., Jenkins, A., et al. 2005, Natur, 435, 629
Takahashi, M. I., Shioya, Y., Taniguchi, Y., et al. 2007, ApJS, 172, 456
Teplitz, H. I., Malkan, M., & McLean, I. S. 1998, ApJ, 506, 519
Toomre, A., & Toomre, J. 1972, ApJ, 178, 623
Trager, S. C., Faber, S. M., Worthey, G., & González, J. J. 2000a, AJ, 120, 165
Trager, S. C., Faber, S. M., Worthey, G., & González, J. J. 2000b, AJ, 119, 1645
van Dokkum, P. G. 2005, AJ, 130, 2647
van Dokkum, P. G., & Brammer, G. 2010, ApJL, 718, 73
van Dokkum, P. G., Franx, M., Fabricant, D., Kelson, D. D., & Illingworth, G. D. 1999, ApJL, 520, 95
Vazdekis, A., Peletier, R. F., Beckman, J. E., & Casuso, E. 1997, ApJS, 111, 203
Villar, V., Gallego, J., Pérez-González, P. G., et al. 2008, ApJ, 677, 169
Villar, V., Gallego, J., Pérez-González, P. G., et al. 2011, ApJ, 740, 47
Whitaker, K. E., Kriek, M., van Dokkum, P. G., et al. 2012, ApJ, 745, 179
Whitaker, K. E., Labbé, Ivo, van Dokkum, P. G., et al. 2011, ApJ, 735, 86
Whitaker, K. E., van Dokkum, P. G., Brammer, G., et al. 2010, ApJ, 719, 1715
Willis, J. P., & Courbin, F. 2005, MNRAS, 357, 1348
Wirth, G. D., Willmer, C. N. A., Amico, P., et al. 2004, AJ, 127, 3121
Wolf, C., Dye, S., Kleinheinrich, M., et al. 2001, A&A, 377, 442
Wolf, C., Meisenheimer, K., Kleinheinrich, M., et al. 2004, A&A, 421, 913
Wolf, C., Wisotzki, L., Borch, A., et al. 2003, A&A, 408, 499
Worthey, G. 1994, ApJS, 95, 107
Worthey, G., Faber, S. M., Gonzalez, J. J., & Burstein, D. 1994, ApJS, 94, 687
Wuyts, S., Franx, M., Cox, T. J., et al. 2009, ApJ, 696, 348
Yan, L., McCarthy, P. J., Weymann, R. J., et al. 2000, AJ, 120, 575
Yates, R. M., Kauffmann, G., & Guo, Q. 2012, MNRAS, 422, 215